

# Connection between zero-energy Yu-Shiba-Rusinov states and $0-\pi$ transitions in magnetic Josephson junctions

Andreas Costa,\* Jaroslav Fabian, and Denis Kochan

*Institute for Theoretical Physics, University of Regensburg, 93040 Regensburg, Germany*

(Dated: December 14, 2024)

We study the bound state spectrum and  $0-\pi$  transitions in ballistic quasi-1D superconductor/ferromagnetic insulator/superconductor (S/FI/S) Josephson junctions. In addition to the Andreev bound states, stemming from the phase coherence, the magnetic barrier gives rise to qualitatively different Yu-Shiba-Rusinov (YSR) bound states with genuine spectral features and spin characteristics. We show that zero-energy YSR states are much more robust against scalar tunneling than their Andreev counterparts and also fingerprint a quantum phase transition from the junctions'  $0$  into the  $\pi$  phase, connected to a measurable reversal of the Josephson current flow; this coincidence persists also in the presence of Rashba spin-orbit coupling.

*Introduction.* Since its discovery, superconductivity evolved into a most influential research area in fundamental science and technology. While the exchange interaction in metals favors parallel spin alignment, giving rise to the magnetic ground state [1], the attractive pairing interaction promotes the formation of Cooper pairs with antiparallel spin [2, 3] in the superconducting phase. The competition of those two antagonistic interactions in one system can lead to interesting physical phenomena [4–6]. Prominent examples are  $\pi$  Josephson junctions [7–15], in which an additional intrinsic  $\pi$  shift reverses the flow of the Josephson current compared to the usual  $0$  state junctions. Recent experiments [6, 16–19] have boosted hopes for controllable engineering of such  $0-\pi$  transitions with applications in superconducting qubits [20], quantum computing [21–23], or spintronics [4, 24, 25].

The phase-coherent coupling between two superconducting electrodes in Josephson junctions leads to coherent Andreev bound states (ABS) [26, 27] inside the superconducting gap, that channel the Josephson current across the system [28]. During the last years, ABS have been mostly studied in Josephson junctions in which the electrodes were coupled by a single quantum dot [29–32]. The recent work of Su *et al.* [33] focused on the phase-coherent coupling via a double quantum dot. The emergent ABS in that system hybridize to novel Andreev molecular states, bringing new dynamics into the field. Adding more quantum dots to the system is expected to launch a new platform for exploring Majorana physics [34–39].

The presence of magnetic impurities in superconductors (S) can break Cooper pairs and create new single particle states in the energy spectrum, the well-known Yu-Shiba-Rusinov (YSR) bound states [40–43]. The characteristics of YSR states have been studied during the last years in several systems, ranging from superconducting substrates hosting magnetic adatoms [44] to normal/superconductor systems connected by nanowires [45, 46], and also in quantum dot-coupled Josephson junc-

tions [47]. In the latter, the interplay of the conventional ABS and the YSR states leads to anomalous electrical transport phenomena [45, 48]. Another interesting feature is attributed to zero-energy YSR states, which can bridge trivial and topological superconductivity [49–51] and fingerprint quantum phase transitions in the junctions' ground state [52].

In this letter, we investigate the subgap bound state spectrum of vertical S/FI/S Josephson junctions with an ultrathin ferromagnetic insulator layer (FI). In contrast to earlier studies treating diffusive metal/superconductor heterojunctions [53, 54], we focus on ballistic junctions. We demonstrate that, apart from the conventional ABS, the presence of magnetic barriers gives rise to additional YSR bound states. Their unique spectral and *spin* characteristics are further tunable either by modulating the scalar or magnetic tunneling strengths, or by changing the superconducting phase difference across the junction. Moreover, we show that such bound states strongly impact the quasiparticle (QP) density of states (DOS) in the system, suppressing coherence peaks near the gap edges. By studying the many-body ground state wave function, we clearly distinguish  $0$  and  $\pi$  phases of the junctions and show that the quantum phase transition from the  $0$  to the  $\pi$  phase [52, 55–60] happens when the bound states cross zero energy. This is consistent with experimental observations in quantum-dot coupled junctions [29, 31, 61–65]. We demonstrate that the above findings remain valid even in the presence of Rashba spin-orbit coupling (SOC) [25, 66] in the leads. A measurable signature of the phase transition is the reversal of the Josephson current. We explain this reversal in terms of tunneling of Cooper pairs via the spectrally distinct ABS and YSR states.

*Theoretical model and bound state spectrum.* We consider a vertical ballistic S/FI/S Josephson junction, consisting of two semi-infinite S regions at  $z < 0$  and  $z > 0$  half-spaces that are separated by a thin delta-like tunnel barrier, simulating scalar and magnetic tunneling; see Fig. 1(a). To analyze the spectral properties of the junction, we model the system in terms of the stationary

\* Corresponding author: andreas.costa@physik.uni-regensburg.de

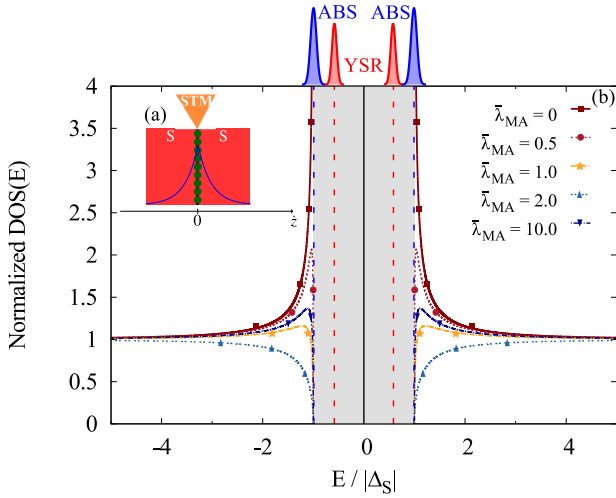


FIG. 1. (a) Josephson junction geometry; two superconductors (S; red) are separated by a thin delta-like ferromagnetic insulator (green dots). (b) Calculated QP DOS for scalar tunneling  $\bar{\lambda}_{\text{SC}} = 2$ , zero phase difference, and various magnetic strengths  $\bar{\lambda}_{\text{MA}}$  with the pronounced coherence peak modulations. The subgap dashed lines schematically illustrate the ABS and YSR bound states; see text for details.

Bogoljubov–de Gennes Hamiltonian [67],

$$\hat{H}_{\text{BdG}} = \begin{bmatrix} \hat{H}_e & \hat{\Delta}_S(z) \\ \hat{\Delta}_S^\dagger(z) & \hat{H}_h \end{bmatrix}. \quad (1)$$

$$\frac{E_n^\pm}{|\Delta_S|} = \pm \sqrt{\frac{(\bar{\lambda}_{\text{SC}}^2 - \bar{\lambda}_{\text{MA}}^2)^2 + 8 \left[ 2 \cos^2 \frac{\phi_S}{2} + \frac{\bar{\lambda}_{\text{SC}}^2}{2} (\cos^2 \frac{\phi_S}{2} + 1) + \frac{\bar{\lambda}_{\text{MA}}^2}{2} \sin^2 \frac{\phi_S}{2} + (-1)^n |\bar{\lambda}_{\text{MA}}| \sqrt{\sin^2 \phi_S + \bar{\lambda}_{\text{SC}}^2 \sin^2 \frac{\phi_S}{2} + \bar{\lambda}_{\text{MA}}^2 \cos^2 \frac{\phi_S}{2}} \right]}{(\bar{\lambda}_{\text{SC}}^2 - \bar{\lambda}_{\text{MA}}^2 + 4)^2 + 16 \bar{\lambda}_{\text{MA}}^2}}, \quad (2)$$

where  $\bar{\lambda}_{\text{SC}} = 2m\lambda_{\text{SC}}/(\hbar^2 q_{\text{F}})$  and  $\bar{\lambda}_{\text{MA}} = 2m\lambda_{\text{MA}}/(\hbar^2 q_{\text{F}})$  represent effective tunneling strengths with respect to the Fermi level (chemical potential  $\mu$ );  $q_{\text{F}} = \sqrt{2m\mu}/\hbar$  stands for the Fermi momentum.

Let us shortly examine the main bound state spectral characteristics. Taking  $\bar{\lambda}_{\text{MA}} \rightarrow 0$ , we recover the conventional Andreev limit [10, 73],

$$E_1^\pm = E_2^\pm = \pm |\Delta_S| \sqrt{\frac{\bar{\lambda}_{\text{SC}}^2 + 4 \cos^2(\phi_S/2)}{\bar{\lambda}_{\text{SC}}^2 + 4}}. \quad (3)$$

Complementary, letting  $\bar{\lambda}_{\text{SC}} \rightarrow 0$  and  $\phi_S \rightarrow 0$ , the spectrum yields the celebrated YSR bound states [40, 41, 43] with energies

$$E_1^\pm = \pm |\Delta_S| \frac{\bar{\lambda}_{\text{MA}}^2 - 4}{\bar{\lambda}_{\text{MA}}^2 + 4} \quad (4)$$

and two remaining states at  $E_2^\pm = \pm |\Delta_S|$ , that coin-

Here,  $\hat{H}_e = (-\hbar^2/2m\nabla^2 - \mu)\hat{\sigma}_0 + (\lambda_{\text{SC}}\hat{\sigma}_0 + \lambda_{\text{MA}}\hat{\sigma}_z)\delta(z) + \hat{H}_{\text{R}}$  represents the single-particle electron Hamiltonian and  $\hat{H}_h = -\hat{\sigma}_y \hat{H}_e^* \hat{\sigma}_y$  its time-reversed hole counterpart. The effect of scalar and magnetic tunneling at the interface is modeled by delta-like potentials [68–70] with the effective coupling strengths  $\lambda_{\text{SC}}$  and  $\lambda_{\text{MA}}$ , respectively, while  $\hat{H}_{\text{R}} = -\lambda_{\text{R}} k_z \hat{\sigma}_y \Theta(z)$  accounts for Rashba SOC in the right lead, realized, for instance, by a semi-conducting electrode with proximity-induced superconductivity [71]. Spin matrices  $\hat{\sigma}_0$  and  $\hat{\sigma}_i$  stand for the  $(2 \times 2)$  identity and the  $i$ -th Pauli matrix. For the sake of simplicity, we assume a symmetric S/FI/S junction with equal QP masses  $m$ , the same chemical potential  $\mu$ , and the transverse  $\hat{z}$ -dependent S order parameter  $\hat{\Delta}_S(z) = |\Delta_S| \hat{\sigma}_0 [\Theta(-z) + e^{i\phi_S} \Theta(z)]$ ;  $\phi_S$  is the macroscopic phase difference between the two superconductors.

The general procedure for finding the eigencharacteristics of the Hamiltonian  $\hat{H}_{\text{BdG}}$ , Eq. (1), is outlined in the SM [72]. In what follows, we focus on quasi-1D junctions for which the thickness in the transverse  $\hat{x}$  and  $\hat{y}$  directions is much shorter than in the longitudinal  $\hat{z}$  direction (2D and 3D junctions essentially bring no new features as demonstrated in the SM [72]). The particle-hole symmetric quasi-1D subgap eigenspectrum  $E_n^\pm$  ( $n = 1, 2$ ) in the absence of Rashba SOC reads

cide with the ABS at  $\phi_S = 0$ , see Eq. (3). For that reason, we will refer to the  $E_1^\pm$  branch as the *Yu-Shiba-Rusinov (YSR)-like* and the  $E_2^\pm$  branch as the *Andreev-like* branch, accordingly.

Figure 2 shows a generic spin-resolved bound state spectrum as a function of  $\phi_S$  for various  $\bar{\lambda}_{\text{MA}}$ . Generally, the Andreev-like branch is always closer to the gap edges than the YSR-like branch, i.e.,  $|E_1^\pm| < |E_2^\pm|$ . This can serve as a spectroscopic fingerprint for distinguishing those subgap states. While the Andreev-like states, Eq. (3), can cross zero energy only for a transparent interface and phase differences  $\phi_S = \pi \pmod{2\pi}$  [73], Eq. (2) suggests that additional magnetic tunneling supports zero-energy YSR-like states in a wide range of tunneling parameters and phase differences. Analyzing Eq. (2), one sees that whenever  $0 \leq \bar{\lambda}_{\text{MA}}^2 - \bar{\lambda}_{\text{SC}}^2 \leq 4$ , there always exists a  $\phi_S$  for which the YSR-like branch  $E_1^\pm$  crosses zero energy (see Fig. 2). The corresponding

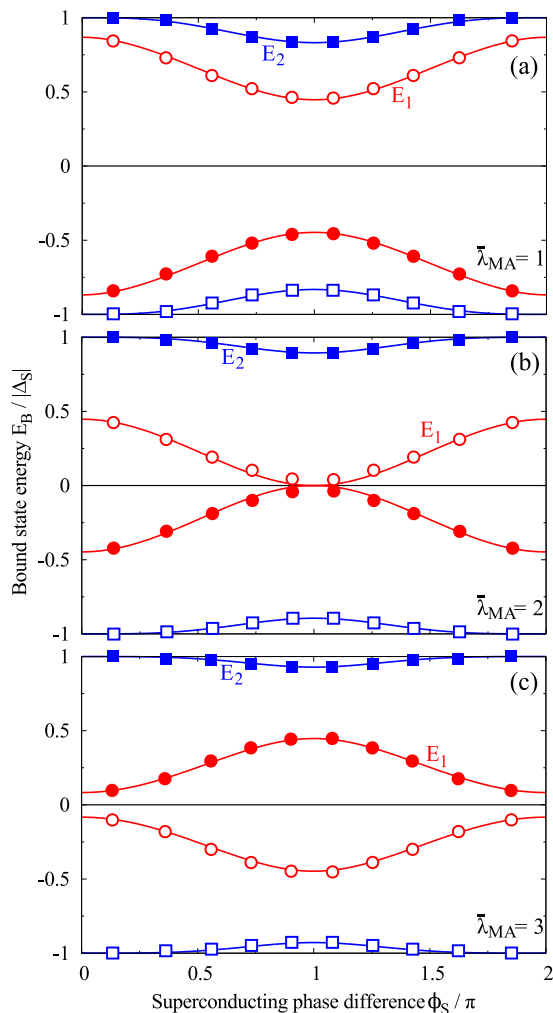


FIG. 2. Spin-resolved bound state energies  $E_1$  and  $E_2$  of the YSR (red) and the Andreev (blue) states as functions of  $\phi_S$  for scalar tunneling  $\bar{\lambda}_{SC} = 2$  and various magnetic tunnelings  $\bar{\lambda}_{MA}$  given in the plots; Rashba SOC is absent. Filled (empty) boxes indicate spin up (down) Andreev states and filled (empty) circles spin up (down) YSR states.

value of  $\phi_S$  comes as a solution of

$$\bar{\lambda}_{MA} = \pm \sqrt{\bar{\lambda}_{SC}^2 + 4 \cos^2(\phi_S/2)}. \quad (5)$$

*Modulation of QP DOS.* The subgap bound states strongly impact the QP DOS in the system. Figure 1(b) shows the calculated DOS for  $\bar{\lambda}_{SC} = 2$  and for different  $\bar{\lambda}_{MA}$ 's at zero phase difference (for methodology, see the SM [72]). Without magnetic tunneling, the subgap spectrum only consists of ABS and the QP spectrum shows the standard BCS-like DOS. With gradually growing  $\bar{\lambda}_{MA}$ , the spectrum also contains YSR states that move to the center of the gap. As a consequence, a part of spectral weight is taken into the gap and the coherence peaks in the BCS-like QP DOS modify. A similar peak structure was identified in quantum-dot experiments aligning the tunnel probe energy with the corresponding bound

states [31, 64]. Raising  $\bar{\lambda}_{MA}$ , the QP spectral peaks become unprecedentedly suppressed and disappear when the YSR states cross zero energy. A further increase of  $\bar{\lambda}_{MA}$  shifts the bound states back towards the gap edges and simultaneously, the QP DOS rises again.

*Qualitative analysis—ground state phase transition.* We see from Fig. 2 that the Andreev-like states do not change spins with evolving  $\phi_S$ , whereas the YSR-like states effectively ‘flip’ spins when crossing zero energy. As expected, reversing the sign of  $\bar{\lambda}_{MA}$  reverses the bound states’ spins. The spin ordering of the bound states reflects important properties of the ground state, which we shortly discuss. Without the delta-like terms in  $\hat{H}_e$  and  $\hat{H}_h$ , for zero Rashba SOC, and for  $\phi_S = 0$ , the BdG Hamiltonian  $\hat{H}_{BdG}$ , Eq. (1), can be easily diagonalized. Denoting by  $\alpha^\dagger$  ( $\alpha$ ) the creation (annihilation) operators for the BdG eigenmodes with positive energies and by  $\beta^\dagger$  ( $\beta$ ) the corresponding operators for the negative energies, the BCS ground state  $|\Omega\rangle$  is a Slater product over the occupied and unoccupied eigenmodes, i.e.,

$$|\Omega\rangle = \prod_{\mathbf{k}} \alpha_{\mathbf{k},\uparrow} \alpha_{-\mathbf{k},\downarrow} \beta_{\mathbf{k},\uparrow}^\dagger \beta_{-\mathbf{k},\downarrow}^\dagger |0\rangle. \quad (6)$$

Here,  $|0\rangle$  represents an ordinary Fermi vacuum.

Let us qualitatively outline what happens with  $|\Omega\rangle$  when adding a delta-like exchange interaction, parameterized by  $\lambda_{MA}$ , to  $\hat{H}_{BdG}$ . For simplicity, let us start with zero  $\lambda_{SC}$  and  $\phi_S$ . Assuming a small positive  $\lambda_{MA}$ , the spin up states have higher energy than their spin down counterparts. This means that the initially degenerate QP eigenmodes would spin split, and form spatially (quasi)localized impurity subgap states. Anticipating the results of Eq. (2) for  $\lambda_{SC} = 0$  and  $\phi_S = 0$ , we denote the localized states with positive energies  $0 < E_1^+ < E_2^+ \simeq |\Delta_S|$  as  $|\psi_{YSR,\downarrow}\rangle$  and  $|\psi_{A,\uparrow}\rangle$ , and states with negative energies  $-\Delta_S \simeq E_2^- < E_1^- < 0$ , as  $|\psi_{A,\downarrow}\rangle$  and  $|\psi_{YSR,\uparrow}\rangle$ , see Fig. 3. Generally, the states  $|\psi_{YSR,\uparrow}\rangle$  and  $|\psi_{YSR,\downarrow}\rangle$  are shifted more towards the center of the gap than  $|\psi_{A,\downarrow}\rangle$  and  $|\psi_{A,\uparrow}\rangle$  for  $\lambda_{MA} > 0$ , and hence become spatially more localized around the impurity. With a further increase of  $\lambda_{MA}$ , the energy of  $|\psi_{YSR,\downarrow}\rangle$  continuously lowers, while that of  $|\psi_{YSR,\uparrow}\rangle$  rises. Before reaching the critical value  $\lambda_{MA}^{\text{crit}} \sim \xi_{\text{BCS}} |\Delta_S|$ , where  $\xi_{\text{BCS}}$  stands for the BCS coherence length,  $|\psi_{YSR,\downarrow}\rangle$  remains unoccupied and  $|\psi_{YSR,\uparrow}\rangle$  occupied, see Fig. 3(a). Denoting the corresponding creation (annihilation) operators for  $|\psi_{A,\sigma}\rangle$  and  $|\psi_{YSR,\sigma}\rangle$  by  $A_\sigma^\dagger$  ( $A_\sigma$ ) and  $Y_\sigma^\dagger$  ( $Y_\sigma$ ), respectively, we expect the ground state of the perturbed system below  $\lambda_{MA}^{\text{crit}}$  in the form

$$|\Omega_{<}\rangle \sim A_\uparrow Y_\downarrow Y_\uparrow^\dagger A_\downarrow^\dagger \prod_{\mathbf{n}} \tilde{\alpha}_{\mathbf{n},\uparrow} \tilde{\alpha}_{-\mathbf{n},\downarrow} \tilde{\beta}_{\mathbf{n},\uparrow}^\dagger \tilde{\beta}_{-\mathbf{n},\downarrow}^\dagger |0\rangle. \quad (7)$$

The tilde operators have the same meaning as before—QP eigenmodes (now perturbed) with energies above and below the S gap [74]. Increasing  $\lambda_{MA}$  over the critical  $\lambda_{MA}^{\text{crit}}$ , the energy of  $|\psi_{YSR,\downarrow}\rangle$  becomes smaller than the energy of  $|\psi_{YSR,\uparrow}\rangle$  and therefore, the relative occupations

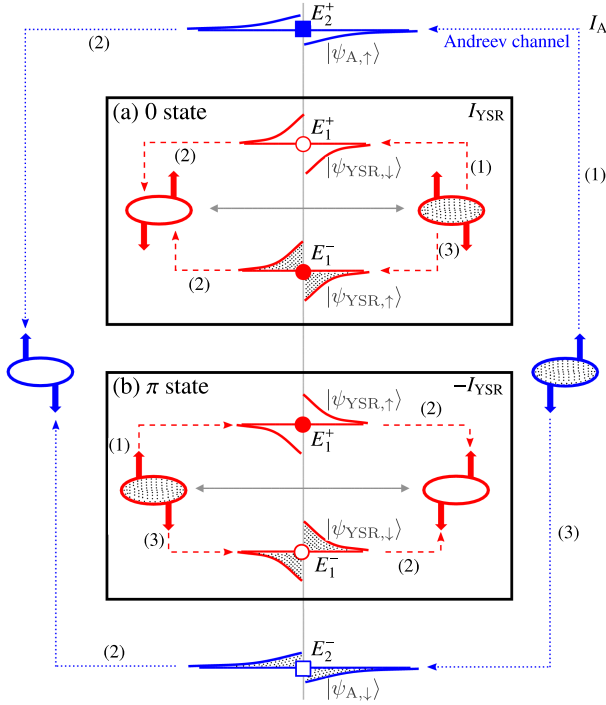


FIG. 3. Schematic picture of 0 and  $\pi$  ground states, and the associated transfer of Cooper pairs. Full (empty) squares/circles display, correspondingly, spin up (down) Andreev/YSR states; the states (with energies  $E_2^\pm$  and  $E_1^\pm$ ) are labeled as  $|\psi_{A,\sigma}\rangle$  and  $|\psi_{YSR,\sigma}\rangle$ . The sketched evanescent tails indicate the spatial electron-hole density difference for a given  $|\psi\rangle$ ; positive (negative) density differences represent a spatial excess of electron (hole) character at the interface. Occupied bound states and Cooper pairs are indicated by shading. The dotted (blue) lines describe the Cooper pair transfer via the Andreev channel (current  $I_A$ ) and the dashed (red) lines via the YSR channel (current  $I_{YSR}$ ). The individual steps (1), (2), and (3) are described in the text. The 0 state junction is displayed in panel (a) and the  $\pi$  state junction in panel (b). The change of the YSR spectral properties at the 0- $\pi$  transition reverses  $I_{YSR}$ , while  $I_A$  remains unchanged.

of both states interchange, see Fig. 3(b). The ground state wave function above  $\lambda_{MA}^{\text{crit.}}$  is now expected to be in the form

$$|\Omega_{>}\rangle \sim A_{\uparrow} Y_{\uparrow} Y_{\downarrow}^{\dagger} A_{\downarrow}^{\dagger} \prod_{\mathbf{n}} \tilde{\alpha}_{\mathbf{n},\uparrow} \tilde{\alpha}_{-\mathbf{n},\downarrow} \tilde{\beta}_{\mathbf{n},\uparrow}^{\dagger} \tilde{\beta}_{-\mathbf{n},\downarrow}^{\dagger} |0\rangle. \quad (8)$$

Obviously, the former ground state  $|\Omega_{<}\rangle$  has a modified spin content inside the gap when compared to  $|\Omega_{>}\rangle$ , so both are in distinct quantum states, which we correspondingly call 0 and  $\pi$  phase. Turning on  $\lambda_{SC}$  and  $\phi_S$ , the bound state energies evolve in a complex way—see Eq. (2) for  $\lambda_{SC} \neq 0$  and  $\phi_S \neq 0$ —nevertheless, crossings at zero energy again indicate changes in the spin ordering of the corresponding ground states. Thus, reversals of the Josephson current at 0- $\pi$  transitions in ballistic S/FI/S junctions are interpreted in terms of a *change of the ground state spin order* (ground state quantum phase transition).

*0- $\pi$  transitions in the Josephson current.* Knowing the phase dependence of the bound state spectrum, we can sum up the contributions from both Andreev and YSR-like states with positive energies to obtain the (dc) Josephson current [28],  $I_J(\phi_S) = -\frac{e}{\hbar} \sum_{n=1}^2 \left[ \left( \frac{\partial E_n^+}{\partial \phi_S} \right) \tanh \left( \frac{E_n^+}{2k_B T} \right) \right]$ ; here,  $e$  stands for the (positive) elementary charge and  $k_B$  for the Boltzmann constant. From the experimental point of view, it would be most common to measure the critical Josephson current  $I^{\text{crit.}} = \max_{\phi_S} \{|I_J(\phi_S)|\}$  and the corresponding critical S phase  $\phi_S^{\text{crit.}}$ . By tuning  $\phi_S$  to its critical value and performing STS/STM spectroscopy measurements in the vicinity of the junction interface, one would be able to explore the spectral properties of the subgap states. Figure 4(a) displays the dependence of  $I^{\text{crit.}}$  on the strengths of scalar and magnetic tunnelings. For each  $\bar{\lambda}_{SC}$ , one finds a  $\bar{\lambda}_{MA}$  at which the sign of the Josephson current reverses, what indicates a transition from the 0 to the  $\pi$  regime. The maximally flowing current in the 0 state is twice as large as in the  $\pi$  state; moreover, as expected, the 0- $\pi$  transition lines coincide with the contours signifying the formation of zero-energy YSR-like states. In Fig. 4(b), we show similar, fully numerical, calculations in the additional presence of moderate Rashba SOC in the right electrode. Modulating the Rashba SOC by electrical gating [75, 76] can efficiently tune the positions of 0- $\pi$  transitions. Nevertheless, there is still a clear coincidence between the 0- $\pi$  transition lines and the zero-energy YSR states, although SOC inevitably introduces an additional intrinsic shift to the current-phase relation. This is causing a slight deviation at weak tunnelings.

*Zero-energy YSR states & reversal of Josephson current.* To connect the zero-energy YSR states—indicating the ground state quantum phase transition—with the reversal of the Josephson current, one needs to know the bound state wave functions. The full calculation is rather technical; see the SM [72]. Here, we qualitatively illustrate the main physical mechanism behind the transition. Figure 3 schematically shows the Andreev (blue dotted lines) and YSR (red dashed lines) channels, transporting Cooper pairs across the barrier. To understand the transport direction of one Cooper pair, we split each occupied and unoccupied bound state into its electron-like and hole-like component and read out the corresponding electron-hole density difference. This is qualitatively illustrated by the sketched evanescent tails in Fig. 3 for the corresponding  $|\psi_{A,\sigma}\rangle$  and  $|\psi_{YSR,\sigma}\rangle$  states. For the ABS, there is always an electron-like excess in the left and a hole-like excess in the right superconductor. This means that the electrons forming a Cooper pair are transferred via the Andreev channel from the right into the left superconductor; numbers (1)–(3) label the individual steps. In step (1), an electron with spin up tunnels to an empty state at positive energy  $E_2^+$ . In step (2), this electron pairs with a spin down electron residing in the occupied state at energy  $E_2^-$ , creating a spin-singlet Cooper pair in the left superconductor. Fi-

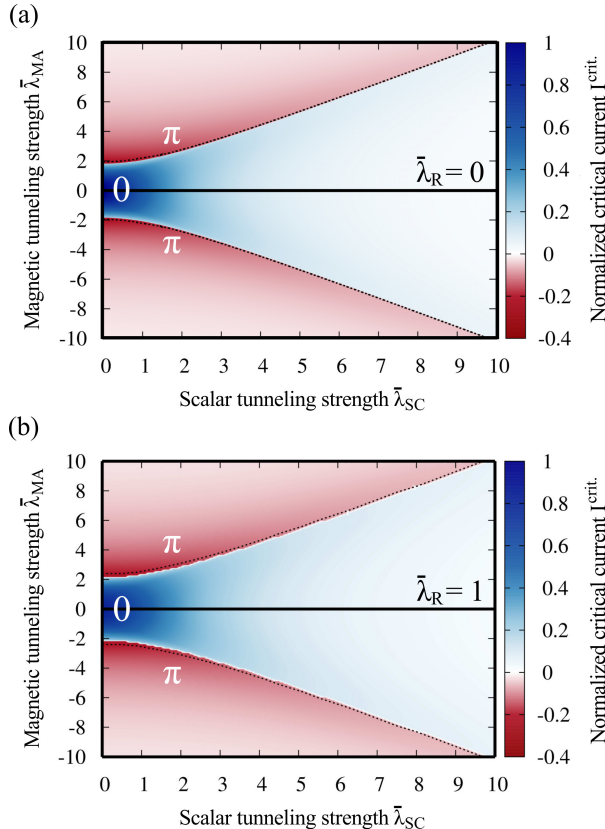


FIG. 4. (a) Contour plot of the normalized critical current [ $eI^{\text{crit}}R_{\text{S}}/(\pi|\Delta_{\text{S}}|)$ ;  $R_{\text{S}}$  is the Sharvin resistance] as a function of  $\bar{\lambda}_{\text{SC}}$  and  $\bar{\lambda}_{\text{MA}}$  in the absence of Rashba SOC at zero temperature. Blue and red regions represent 0 and  $\pi$  junction regimes with positive and negative  $I^{\text{crit}}$ . The transition lines separating the two phases are displayed by white borderlines; the parameters at which zero-energy YSR states emerge are shown by dashed lines. (b) Same calculations in the additional presence of moderate Rashba SOC  $\bar{\lambda}_{\text{R}} = m\lambda_{\text{R}}/(\hbar^2q_{\text{F}}) = 1$ .

nally, the remaining electron from the initial Cooper pair fills the vacant state at  $E_2^-$ . The situation for the YSR

channel is different. In the 0 state, Fig. 3(a), the YSR states show also electron-like excess in the left and hole-like excess in the right superconductor. Hence, the previous transport mechanism holds and Cooper pairs are also transferred from right to left. In total, both current contributions add together  $I_{\text{A}} + I_{\text{YSR}}$ . In contrast, the spin-resolved electron and hole content of the YSR states spatially change in the  $\pi$  state and therefore, the YSR states now drive Cooper pairs from left to right, i.e., against the direction of the Andreev channel. The total current is then  $I_{\text{A}} - I_{\text{YSR}}$ . Since the transition probabilities of the activation step (1) are proportional to  $e^{-E_{\pi}^+/|\Delta_{\text{S}}|}$  and  $E_1^+ < E_2^+$ , the YSR contribution to the current is generally dominant and therefore, a reversal of  $I_{\text{YSR}}$  at the 0- $\pi$  transition point reverses also the total Josephson current. This qualitative explanation of the underlying physical mechanism is fully consistent with the numerical calculations presented in Fig. 4.

*Summary.* We analyzed the spectral and transport characteristics associated with Andreev and YSR sub-gap states in magnetic Josephson junctions in terms of experimentally tunable parameters and showed that certain combinations of these parameters lead to zero-energy YSR states. Such states serve as a clear fingerprint of a quantum phase transition in the junctions' ground state. In particular, we demonstrated that this phase transition coincides with the 0- $\pi$  transition in the junctions, reversing the direction of the Josephson current. The outlined coincidence between zero-energy YSR states and 0- $\pi$  transitions persists also in the presence of Rashba SOC in one of the junction electrodes.

## ACKNOWLEDGMENTS

This work was supported by DFG SFB Grant No. 689 and DFG SFB Grant No. 1277. This project has received funding from the European Union's Horizon 2020 research and innovation programme under Grant agreement No. 696656 and the International Doctorate Program Topological Insulators of the Elite Network of Bavaria.

- 
- [1] E. C. Stoner, Proceedings of the Royal Society of London A: Mathematical, Physical and Engineering Sciences **169**, 339 (1939).
  - [2] J. Bardeen, L. N. Cooper, and J. R. Schrieffer, Phys. Rev. **106**, 162 (1957).
  - [3] J. Bardeen, L. N. Cooper, and J. R. Schrieffer, Phys. Rev. **108**, 1175 (1957).
  - [4] M. Eschrig, Phys. Today **64**, 43 (2011).
  - [5] J. Linder and J. W. A. Robinson, Nature Phys. **11**, 307 (2015).
  - [6] E. C. Gingrich, B. M. Niedzielski, J. A. Glick, Y. Wang, D. L. Miller, R. Loloee, W. P. Pratt Jr, and N. O. Birge, Nat. Phys. **12**, 564 (2016).
  - [7] L. N. Bulaevskii, V. V. Kuzii, and A. A. Sobyenin, Pis'ma Zh. Eksp. Teor. Fiz. **25**, 314 (1977); JETP Lett. **25**, 290 (1977).
  - [8] A. I. Buzdin, L. N. Bulaevskii, and S. V. Panyukov, Pis'ma Zh. Eksp. Teor. Fiz. **35**, 147 (1982); JETP Lett. **35**, 178 (1982).
  - [9] A. V. Andreev, A. I. Buzdin, and R. M. Osgood, Phys. Rev. B **43**, 10124 (1991).
  - [10] A. A. Golubov, M. Y. Kupriyanov, and E. Il'ichev, Rev. Mod. Phys. **76**, 411 (2004).
  - [11] A. I. Buzdin, Rev. Mod. Phys. **77**, 935 (2005).
  - [12] F. S. Bergeret, A. F. Volkov, and K. B. Efetov, Rev. Mod. Phys. **77**, 1321 (2005).

- [13] G. Annunziata, H. Enoksen, J. Linder, M. Cuoco, C. Noce, and A. Sudbø, *Phys. Rev. B* **83**, 144520 (2011).
- [14] O. Vávra, S. Gaži, D. S. Golubović, I. Vávra, J. Dérer, J. Verbeeck, G. Van Tendeloo, and V. V. Moshchalkov, *Phys. Rev. B* **74**, 020502 (2006).
- [15] A. Costa, P. Högl, and J. Fabian, *Phys. Rev. B* **95**, 024514 (2017).
- [16] V. V. Ryazanov, V. A. Oboznov, A. Y. Rusanov, A. V. Veretennikov, A. A. Golubov, and J. Aarts, *Phys. Rev. Lett.* **86**, 2427 (2001).
- [17] T. Kontos, M. Aprili, J. Lesueur, F. Genêt, B. Stephanidis, and R. Boursier, *Phys. Rev. Lett.* **89**, 137007 (2002).
- [18] J. W. A. Robinson, S. Piano, G. Burnell, C. Bell, and M. G. Blamire, *Phys. Rev. Lett.* **97**, 177003 (2006).
- [19] A. K. Feofanov, V. A. Oboznov, V. V. Bol'ginov, J. Lisenfeld, S. Poletto, V. V. Ryazanov, A. N. Rossolenko, M. Khabipov, D. Balashov, A. B. Zorin, P. N. Dmitriev, V. P. Koshelets, and A. V. Ustinov, *Nat. Phys.* **6**, 593 (2010).
- [20] T. Yamashita, K. Tanikawa, S. Takahashi, and S. Maekawa, *Phys. Rev. Lett.* **95**, 097001 (2005).
- [21] L. B. Ioffe, V. B. Geshkenbein, M. V. Feigel'man, A. L. Fauchère, and G. Blatter, *Nature* **398**, 679 (1999).
- [22] J. E. Mooij, T. P. Orlando, L. Levitov, L. Tian, C. H. van der Wal, and S. Lloyd, *Science* **285**, 1036 (1999).
- [23] M. H. Devoret and R. J. Schoelkopf, *Science* **339**, 1169 (2013).
- [24] I. Žutić, J. Fabian, and S. Das Sarma, *Rev. Mod. Phys.* **76**, 323 (2004).
- [25] J. Fabian, A. Matos-Abiague, C. Ertler, P. Stano, and I. Žutić, *Acta Phys. Slovaca* **57**, 565 (2007).
- [26] A. F. Andreev, *J. Exp. Theor. Phys.* **19**, 1228 (1964); *Zh. Eksp. Teor. Fiz.* **46**, 1823 (1964).
- [27] A. F. Andreev, *J. Exp. Theor. Phys.* **22**, 455 (1966); *Zh. Eksp. Teor. Fiz.* **49**, 655 (1966).
- [28] I. O. Kulik, *Zh. Eksp. Teor. Fiz.* **57**, 1745 (1969); *J. Exp. Theor. Phys.* **30**, 944 (1970).
- [29] E. J. H. Lee, X. Jiang, M. Houzet, R. Aguado, C. M. Lieber, and S. De Franceschi, *Nat. Nanotechnol.* **9**, 79 (2014).
- [30] R. Delagrangé, D. J. Luitz, R. Weil, A. Kasumov, V. Meden, H. Bouchiat, and R. Deblock, *Phys. Rev. B* **91**, 241401 (2015).
- [31] S. Li, N. Kang, P. Caroff, and H. Q. Xu, *Phys. Rev. B* **95**, 014515 (2017).
- [32] D. J. van Woerkom, A. Proutski, B. van Heck, D. Bouman, J. I. Vayrynen, L. I. Glazman, P. Krogstrup, J. Nygård, L. P. Kouwenhoven, and A. Geresdi, *Nat. Phys.* (2017).
- [33] Z. Su, A. B. Tacla, M. Hocevar, D. Car, S. R. Plissard, E. P. A. M. Bakkers, A. J. Daley, D. Pekker, and S. M. Frolov, *Nat. Commun.* **8** (2017).
- [34] V. Mourik, K. Zuo, S. M. Frolov, S. R. Plissard, E. P. A. M. Bakkers, and L. P. Kouwenhoven, *Science* **336**, 1003 (2012).
- [35] S. Nadj-Perge, I. K. Drozdov, J. Li, H. Chen, S. Jeon, J. Seo, A. H. MacDonald, B. A. Bernevig, and A. Yazdani, *Science* **346**, 602 (2014).
- [36] Y. Oreg, G. Refael, and F. von Oppen, *Phys. Rev. Lett.* **105**, 177002 (2010).
- [37] M. Duckheim and P. W. Brouwer, *Phys. Rev. B* **83**, 054513 (2011).
- [38] L. P. Rokhinson, X. Liu, and J. K. Furdyna, *Nature Phys.* **8**, 795 (2012).
- [39] L. Fu and C. L. Kane, *Phys. Rev. Lett.* **100**, 096407 (2008).
- [40] L. Yu, *Acta Phys. Sin.* **21**, 75 (1965).
- [41] H. Shiba, *Progr. Theoret. Phys.* **40**, 435 (1968).
- [42] H. Shiba and T. Soda, *Progr. Theoret. Phys.* **41**, 25 (1969).
- [43] A. I. Rusinov, *ZhETF Pis. Red.* **9**, 85 (1968).
- [44] M. Ruby, Y. Peng, F. von Oppen, B. W. Heinrich, and K. J. Franke, *Phys. Rev. Lett.* **117**, 186801 (2016).
- [45] R. Žitko, J. S. Lim, R. López, and R. Aguado, *Phys. Rev. B* **91**, 045441 (2015).
- [46] A. Jellinggaard, K. Grove-Rasmussen, M. H. Madsen, and J. Nygård, *Phys. Rev. B* **94**, 064520 (2016).
- [47] G. Kiršanskas, M. Goldstein, K. Flensberg, L. I. Glazman, and J. Paaske, *Phys. Rev. B* **92**, 235422 (2015).
- [48] E. J. H. Lee, X. Jiang, R. Aguado, G. Katsaros, C. M. Lieber, and S. De Franceschi, *Phys. Rev. Lett.* **109**, 186802 (2012).
- [49] J. D. Sau and E. Demler, *Phys. Rev. B* **88**, 205402 (2013).
- [50] F. Pientka, Y. Peng, L. Glazman, and F. von Oppen, *Phys. Scripta* **2015**, 014008 (2015).
- [51] N. Hatter, B. W. Heinrich, M. Ruby, J. I. Pascual, and K. J. Franke, *Nat. Commun.* (2015).
- [52] A. Sakurai, *Progr. Theor. Exp. Phys.* **44**, 1472 (1970).
- [53] D. Persson, O. Shevtsov, T. Löfwander, and M. Fogelström, *Phys. Rev. B* **92**, 245430 (2015).
- [54] D. Persson, O. Shevtsov, T. Löfwander, and M. Fogelström, *Phys. Rev. B* **94**, 155424 (2016).
- [55] K. Satori, H. Shiba, O. Sakai, and Y. Shimizu, *J. Phys. Soc. Jpn.* **61**, 3239 (1992).
- [56] J. Simonin and R. Allub, *Phys. Rev. Lett.* **74**, 466 (1995).
- [57] M. I. Salkola, A. V. Balatsky, and J. R. Schrieffer, *Phys. Rev. B* **55**, 12648 (1997).
- [58] A. V. Balatsky, I. Vekhter, and J.-X. Zhu, *Rev. Mod. Phys.* **78**, 373 (2006).
- [59] J. Bauer, A. Oguri, and A. C. Hewson, *J. Phys. Condens. Matter* **19**, 486211 (2007).
- [60] W.-F. Tsai, Y.-Y. Zhang, C. Fang, and J. Hu, *Phys. Rev. B* **80**, 064513 (2009).
- [61] R. S. Deacon, Y. Tanaka, A. Oiwa, R. Sakano, K. Yoshida, K. Shibata, K. Hirakawa, and S. Tarucha, *Phys. Rev. Lett.* **104**, 076805 (2010).
- [62] K. J. Franke, G. Schulze, and J. I. Pascual, *Science* **332**, 940 (2011).
- [63] B.-K. Kim, Y.-H. Ahn, J.-J. Kim, M.-S. Choi, M.-H. Bae, K. Kang, J. S. Lim, R. López, and N. Kim, *Phys. Rev. Lett.* **110**, 076803 (2013).
- [64] A. Kumar, M. Gaim, D. Steininger, A. L. Yeyati, A. Martín-Rodero, A. K. Hüttel, and C. Strunk, *Phys. Rev. B* **89**, 075428 (2014).
- [65] A. Assouline, C. Feuillet-Palma, A. Zimmers, H. Aubin, M. Aprili, and J.-C. Harmand, *Phys. Rev. Lett.* **119**, 097701 (2017).
- [66] Y. A. Bychkov and E. I. Rashba, *J. Phys. C* **17**, 6039 (1984).
- [67] P. G. De Gennes, *Superconductivity of Metals and Alloys* (Addison Wesley, 1989).
- [68] M. J. M. De Jong and C. W. J. Beenakker, *Phys. Rev. Lett.* **74**, 1657 (1995).
- [69] I. Žutić and O. T. Valls, *Phys. Rev. B* **60**, 6320 (1999).
- [70] I. Žutić and O. T. Valls, *Phys. Rev. B* **61**, 1555 (2000).
- [71] Y. Zhi-Hong, Y. Yong-Hong, and W. Jun, *Chinese Physics B* **21**, 057402 (2012).
- [72] See attached Supplemental Material for more details.

- [73] C. W. J. Beenakker, Phys. Rev. Lett. **67**, 3836 (1991).
- [74] Since momentum is not a good quantum number, we rather use a general index  $\mathbf{n}$  that labels perturbed eigenmodes above and below the S gap.
- [75] J. Nitta, T. Akazaki, H. Takayanagi, and T. Enoki, Phys. Rev. Lett. **78**, 1335 (1997).
- [76] T. Koga, J. Nitta, T. Akazaki, and H. Takayanagi, Phys. Rev. Lett. **89**, 046801 (2002).

# SUPPLEMENTAL MATERIAL

## Connection between zero-energy Yu-Shiba-Rusinov states and $0-\pi$ transitions in magnetic Josephson junctions

Andreas Costa, Jaroslav Fabian, and Denis Kochan  
*Institute for Theoretical Physics, University of Regensburg, 93040 Regensburg, Germany*

In this Supplemental Material, we present the computational details not included into the manuscript and additional model calculations for a richer set of parameter combinations, which are useful to get a deeper understanding of the physical background.

### I. THEORETICAL MODEL AND BOUND STATE SPECTRUM – COMPUTATIONAL DETAILS

We consider a vertical ballistic S/FI/S Josephson junction consisting of two semi-infinite S regions, spanning  $z < 0$  and  $z > 0$  half-spaces, respectively. They are separated by a thin delta-like ferromagnetic insulator (FI) layer. The junction is schematically depicted in Fig. S1. In order to analyze its spectral properties, we model the system in terms of stationary Bogoljubov–de Gennes equations [S1], which in particle-hole Nambu space  $\Psi = [\psi_\uparrow, \psi_\downarrow, \psi_\downarrow^\dagger, -\psi_\uparrow^\dagger]^\top$  read

$$\begin{bmatrix} \hat{H}_e & \hat{\Delta}_S(z) \\ \hat{\Delta}_S^\dagger(z) & \hat{H}_h \end{bmatrix} \Psi(\mathbf{r}) = E\Psi(\mathbf{r}). \quad (\text{S1})$$

The electron and hole Hamiltonians including perturbation terms and the superconducting order parameter are provided in the manuscript.

Since the wave vector  $\mathbf{k}_\parallel = [k_x, k_y, 0]^\top$  parallel to the interface is conserved, the bound state solution ansatz for Eq. (S1) reads  $\Psi(\mathbf{r}) = \Psi(z) e^{i\mathbf{k}_\parallel \cdot \mathbf{r}_\parallel}$ , where  $\mathbf{r}_\parallel = [x, y, 0]^\top$ . The unknown transverse wave function  $\Psi(z)$  satisfies a reduced one-dimensional Bogoljubov–de Gennes scattering problem, whose general solution can be written for the left ( $z < 0$ ) and right ( $z > 0$ ) S regions as

$$\Psi(z < 0) = \mathcal{A} e^{-iq_{ez}z} \begin{bmatrix} u \\ 0 \\ v \\ 0 \end{bmatrix} + \mathcal{B} e^{-iq_{ez}z} \begin{bmatrix} 0 \\ u \\ 0 \\ v \end{bmatrix} + \mathcal{C} e^{+iq_{hz}z} \begin{bmatrix} v \\ 0 \\ u \\ 0 \end{bmatrix} + \mathcal{D} e^{+iq_{hz}z} \begin{bmatrix} 0 \\ v \\ 0 \\ u \end{bmatrix} \quad (\text{S2})$$

and

$$\Psi(z > 0) = \mathcal{E} e^{+iq_{ez}z} \begin{bmatrix} ue^{i\phi_S} \\ 0 \\ v \\ 0 \end{bmatrix} + \mathcal{F} e^{+iq_{ez}z} \begin{bmatrix} 0 \\ ue^{i\phi_S} \\ 0 \\ v \end{bmatrix} + \mathcal{G} e^{-iq_{hz}z} \begin{bmatrix} ve^{i\phi_S} \\ 0 \\ u \\ 0 \end{bmatrix} + \mathcal{J} e^{-iq_{hz}z} \begin{bmatrix} 0 \\ ve^{i\phi_S} \\ 0 \\ u \end{bmatrix}. \quad (\text{S3})$$

Along with that ansatz yielding a solution  $\Psi(z)$  with positive energy  $E > 0$ , one has also a second, functionally independent solution  $\tilde{\Psi}(z)$  belonging to the negative energy manifold that can be obtained from  $\Psi(z)$  when interchanging  $u$  to  $-v^*$  and  $v$  to  $u^*$  in the Nambu spinors. Above,  $u = u(E)$  and  $v = v(E)$  are the conventional BCS coherence factors that satisfy

$$u(E) = \sqrt{\frac{1}{2} \left( 1 + \sqrt{1 - \frac{|\Delta_S|^2}{E^2}} \right)} = \sqrt{1 - v(E)^2}. \quad (\text{S4})$$

Since we are looking for the bound state (evanescent) solutions only, the wave function ansatz in Eqs. (S2) and (S3) does not account for an incoming wave. Moreover, the  $\hat{z}$  projections of the wave vectors for electron-like and hole-like quasiparticles,

$$q_{ez}(E) = \sqrt{q_F^2 + \frac{2m}{\hbar^2} \sqrt{E^2 - |\Delta_S|^2} - |\mathbf{k}_\parallel|^2} \quad \text{and} \quad q_{hz}(E) = \sqrt{q_F^2 - \frac{2m}{\hbar^2} \sqrt{E^2 - |\Delta_S|^2} - |\mathbf{k}_\parallel|^2}, \quad (\text{S5})$$

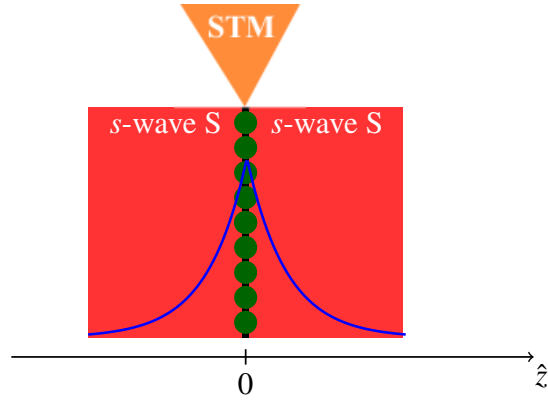


FIG. S1. Schematic sketch of the considered S/FI/S Josephson junction; STM spectroscopy can be used to study the Andreev and YSR bound states close to the interface.

already contain an evanescent imaginary part while  $-|\Delta_S| < E < |\Delta_S|$ ;  $q_F = \sqrt{2m\mu}/\hbar$  stands for the Fermi momentum. Because of the similarities with the true scattering problem, the wave amplitudes  $\mathcal{A}$  and  $\mathcal{B}$  in Eq. (S2) resemble electron-like specular reflection with and without spin flip, and  $\mathcal{C}$  and  $\mathcal{D}$  their Andreev reflected hole-like counterparts. In the same way, the coefficients  $\mathcal{E}$ ,  $\mathcal{F}$ ,  $\mathcal{G}$ , and  $\mathcal{J}$  in Eq. (S3) stand for spin-resolved transmission amplitudes in the right superconductor. To obtain them, we need to fulfill the interfacial ( $z = 0$ ) matching conditions

$$\Psi(z)|_{z=0_-} = \Psi(z)|_{z=0_+}, \quad (\text{S6})$$

$$\left\{ \left[ \frac{\hbar^2}{2m} \frac{d}{dz} + \lambda_{\text{SC}} \right] \boldsymbol{\eta} + \lambda_{\text{MA}} \boldsymbol{\omega} \right\} \Psi(z)|_{z=0_-} = \frac{\hbar^2}{2m} \frac{d}{dz} \boldsymbol{\eta} \Psi(z)|_{z=0_+}, \quad (\text{S7})$$

where  $\boldsymbol{\eta}$  and  $\boldsymbol{\omega}$  are diagonal ( $4 \times 4$ ) matrices; particularly  $\boldsymbol{\eta} = \text{diag}[\hat{\sigma}_0, -\hat{\sigma}_0]$  and  $\boldsymbol{\omega} = \text{diag}[\hat{\sigma}_z, \hat{\sigma}_z]$ . It turns out that Eqs. (S6)–(S7) represent a homogeneous system of eight linear equations for the unknown wave function amplitudes  $\mathcal{A}, \dots, \mathcal{J}$ . To obtain a nontrivial solution, the determinant of the system's coefficient matrix must be zero, what gives a secular equation for the bound state energies of Eq. (S1).

Numerically, we are in a position to compute the bound state spectrum for a generic S/FI/S Josephson junction. Nevertheless, to give full analytical solutions, we first restrict ourselves to quasi-1D junctions for which the thickness in  $\hat{x}$  and  $\hat{y}$  directions is much shorter than in  $\hat{z}$  direction, or equivalently that  $\mathbf{k}_{\parallel} \rightarrow \mathbf{0}$ , and Rashba SOC in the leads is absent. Under these assumptions, we obtain four different solutions  $E_n^{\pm}$  ( $n = 1, 2$ ) for the bound state energies inside the S gap,

$$E_n^{\pm} = \pm |\Delta_S| \left\{ \frac{2 \left( \bar{\lambda}_{\text{SC}}^2 - \bar{\lambda}_{\text{MA}}^2 + 4 \right) \cos \phi_S + \bar{\lambda}_{\text{SC}}^4 + 2\bar{\lambda}_{\text{MA}}^2 + \bar{\lambda}_{\text{MA}}^4 - 2\bar{\lambda}_{\text{SC}}^2 \left( \bar{\lambda}_{\text{MA}}^2 - 3 \right) + 8}{\left( \bar{\lambda}_{\text{SC}}^2 - \bar{\lambda}_{\text{MA}}^2 + 4 \right)^2 + 16\bar{\lambda}_{\text{MA}}^2} + 4(-1)^n \frac{\sqrt{2\bar{\lambda}_{\text{MA}}^2 \left[ 1 + \bar{\lambda}_{\text{SC}}^2 + \bar{\lambda}_{\text{MA}}^2 + \left( \bar{\lambda}_{\text{MA}}^2 - \bar{\lambda}_{\text{SC}}^2 \right) \cos \phi_S - \cos(2\phi_S) \right]}}{\left( \bar{\lambda}_{\text{SC}}^2 - \bar{\lambda}_{\text{MA}}^2 + 4 \right)^2 + 16\bar{\lambda}_{\text{MA}}^2} \right\}^{1/2}. \quad (\text{S8})$$

By using basic trigonometric identities, one can immediately bring this result into the more compact form given by Eq. (2) in the manuscript. Obviously, the bound state spectrum  $E_n^{\pm}$  is symmetric (superscript  $\pm$ ) with respect to the center of the S gap and depends only on the macroscopic phase difference  $\phi_S$  and the two dimensionless parameters  $\bar{\lambda}_{\text{SC}} = 2m\lambda_{\text{SC}}/(\hbar^2 q_F)$  and  $\bar{\lambda}_{\text{MA}} = 2m\lambda_{\text{MA}}/(\hbar^2 q_F)$ , representing effective strengths of scalar and magnetic tunneling, respectively.

Let us note that the secular bound state equation originating from the matching conditions, Eqs. (S6)–(S7), is not a simple polynomial of eighth degree since the coherence factors  $u(E)$  and  $v(E)$  contain square roots and lead to a transcendental equation. Therefore, we only obtain four independent bound state energies instead of eight solutions one would typically expect for a polynomial of eighth order. Moreover, the interfacial impurity perturbations entering the BdG equation are diagonal in the spin space and therefore, one can introduce a reduced spin-resolved Nambu

basis (in the absence of Rashba SOC in the leads), labeled by  $\sigma = \uparrow = +1$  and  $\sigma = \downarrow = -1$ . In this case, the original bound state ansatz can be recast as

$$\Psi_\sigma(z < 0) = \Psi_\sigma^e(z < 0) + \Psi_\sigma^h(z < 0) = a_\sigma e^{-iq_{ez}z} \begin{bmatrix} u \\ v \end{bmatrix} + b_\sigma e^{+iq_{hz}z} \begin{bmatrix} v \\ u \end{bmatrix} \quad (\text{S9})$$

and

$$\Psi_\sigma(z > 0) = \Psi_\sigma^e(z > 0) + \Psi_\sigma^h(z > 0) = c_\sigma e^{+iq_{ez}z} \begin{bmatrix} ue^{i\phi_S} \\ v \end{bmatrix} + d_\sigma e^{-iq_{hz}z} \begin{bmatrix} ve^{i\phi_S} \\ u \end{bmatrix}, \quad (\text{S10})$$

where we explicitly also separated the electron-like and hole-like components for reasons which will become clear later. The matching conditions then read

$$\Psi_\sigma(z)|_{z=0_-} = \Psi_\sigma(z)|_{z=0_+}, \quad (\text{S11})$$

$$\left\{ \left[ \frac{\hbar^2}{2m} \frac{d}{dz} + \lambda_{\text{SC}} \right] \text{diag}[1, -1] + \lambda_{\text{MA}} \text{diag}[\sigma, \sigma] \right\} \Psi_\sigma(z)|_{z=0_-} = \frac{\hbar^2}{2m} \frac{d}{dz} \text{diag}[1, -1] \Psi_\sigma(z)|_{z=0_+}. \quad (\text{S12})$$

Using the fact that  $\text{Im}[q_{ez}(E_B)] = -\text{Im}[q_{hz}(E_B)]$  for bound state energies  $|E_B| < |\Delta_S|$ , see Eq. (S5), the normalization of the wave functions, Eqs. (S9)–(S10), requires

$$\begin{aligned} 1 &\stackrel{(!)}{=} \left[ |u(E_B)|^2 + |v(E_B)|^2 \right] \left\{ \left[ |a_\sigma(E_B)|^2 + |b_\sigma(E_B)|^2 \right] + \left[ |c_\sigma(E_B)|^2 + |d_\sigma(E_B)|^2 \right] \right\} \int_0^\infty dz e^{-2\text{Im}[q_{ez}(E_B)]z} \\ &= \frac{|u(E_B)|^2 + |v(E_B)|^2}{2\text{Im}[q_{ez}(E_B)]} \left[ |a_\sigma(E_B)|^2 + |b_\sigma(E_B)|^2 + |c_\sigma(E_B)|^2 + |d_\sigma(E_B)|^2 \right]. \end{aligned} \quad (\text{S13})$$

Continuity of the wave functions at the interface, Eq. (S11), relates the coefficients  $c_\sigma(E_B)$  and  $d_\sigma(E_B)$  in the right superconductor to  $a_\sigma(E_B)$  and  $b_\sigma(E_B)$  in the left superconductor, particularly,

$$c_\sigma(E_B) = \alpha_1(E_B) a_\sigma(E_B) + \beta_1(E_B) b_\sigma(E_B), \quad (\text{S14})$$

$$d_\sigma(E_B) = \alpha_2(E_B) a_\sigma(E_B) + \beta_2(E_B) b_\sigma(E_B), \quad (\text{S15})$$

where

$$\alpha_1(E_B) = \frac{e^{-i\phi_S} - v(E_B)^2/u(E_B)^2}{1 - v(E_B)^2/u(E_B)^2}, \quad \beta_1(E_B) = \frac{v(E_B)/u(E_B) \cdot [e^{-i\phi_S} - 1]}{1 - v(E_B)^2/u(E_B)^2}, \quad (\text{S16})$$

$$\alpha_2(E_B) = \frac{v(E_B)/u(E_B) \cdot [1 - e^{-i\phi_S}]}{1 - v(E_B)^2/u(E_B)^2}, \quad \beta_2(E_B) = \frac{1 - v(E_B)^2/u(E_B)^2 \cdot e^{-i\phi_S}}{1 - v(E_B)^2/u(E_B)^2}. \quad (\text{S17})$$

Applying the remaining boundary condition, Eq. (S12), we get  $b_\sigma(E_B)$  in terms of  $a_\sigma(E_B)$ , i.e.,

$$b_\sigma(E_B) = \gamma_\sigma(E_B) a_\sigma(E_B), \quad (\text{S18})$$

where  $\gamma_\sigma(E_B)$  reads

$$\gamma_\sigma(E_B) = - \frac{\left[ -\frac{q_{ez}(E_B)}{q_F} - i\bar{\lambda}_{\text{SC}} - i\sigma\bar{\lambda}_{\text{MA}} - \frac{q_{ez}(E_B)}{q_F} \cdot \alpha_1(E_B)e^{i\phi_S} \right] u(E_B) + \frac{q_{hz}(E_B)}{q_F} \cdot \alpha_2(E_B)e^{i\phi_S} v(E_B)}{\left[ \frac{q_{hz}(E_B)}{q_F} - i\bar{\lambda}_{\text{SC}} - i\sigma\bar{\lambda}_{\text{MA}} + \frac{q_{hz}(E_B)}{q_F} \cdot \gamma_2(E_B)e^{i\phi_S} \right] v(E_B) - \frac{q_{ez}(E_B)}{q_F} \cdot \gamma_1(E_B)e^{i\phi_S} u(E_B)}. \quad (\text{S19})$$

Eliminating the coefficients  $b_\sigma(E_B)$ ,  $c_\sigma(E_B)$ , and  $d_\sigma(E_B)$  in the normalization condition, Eq. (S13), by inserting Eqs. (S14), (S15), and (S18), we finally obtain

$$|a_\sigma(E_B)|^2 = \frac{2\text{Im}[q_{ez}(E_B)] / \left[ |u(E_B)|^2 + |v(E_B)|^2 \right]}{\left[ 1 + |\gamma_\sigma(E_B)|^2 + |\alpha_1(E_B) + \beta_1(E_B)\gamma_\sigma(E_B)|^2 + |\alpha_2(E_B) + \beta_2(E_B)\gamma_\sigma(E_B)|^2 \right]} \quad (\text{S20})$$

for the square of the absolute value of  $a_\sigma(E_B)$ . Going back with the same set of equations, we would consecutively get all remaining coefficients  $b_\sigma(E_B)$ ,  $c_\sigma(E_B)$ , and  $d_\sigma(E_B)$ .

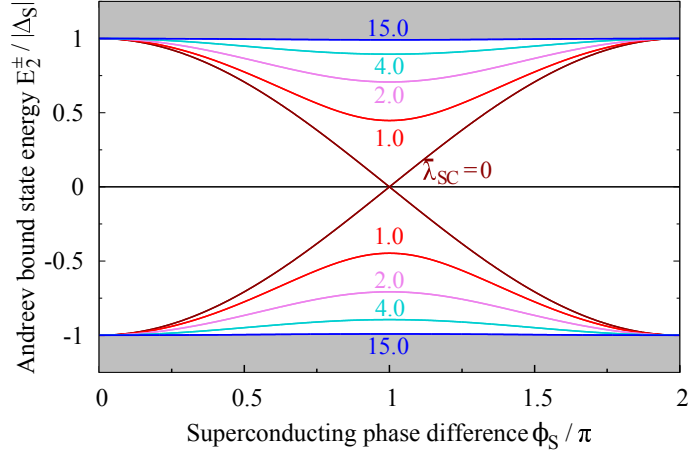


FIG. S2. Andreev bound state energies as a function of  $\phi_S$  for junctions without interfacial magnetic tunneling ( $\bar{\lambda}_{MA} = 0$ ) and Rashba SOC. Different scalar tunnelings  $\bar{\lambda}_{SC}$  are color coded; all states are doubly spin-degenerate.

In the manuscript, we introduced electron-hole density differences to explain the connection between zero-energy YSR-like states and the Josephson current reversing  $0-\pi$  transitions. To obtain those differences,  $|\Psi_\sigma^e(z)|^2 - |\Psi_\sigma^h(z)|^2$ , at an energy  $E_B$  corresponding either to an Andreev or a YSR-like state, we use

$$|\Psi_\sigma^e(z \leq 0)|^2 = \left[ |u(E_B)|^2 + |v(E_B)|^2 \right] |a_\sigma(E_B)|^2 e^{2\text{Im}[q_{ez}(E_B)]z} \quad (\text{S21})$$

and

$$|\Psi_\sigma^h(z \leq 0)|^2 = \left[ |u(E_B)|^2 + |v(E_B)|^2 \right] |b_\sigma(E_B)|^2 e^{2\text{Im}[q_{ez}(E_B)]z} \quad (\text{S22})$$

valid in the left superconductor, and

$$|\Psi_\sigma^e(z \geq 0)|^2 = \left[ |u(E_B)|^2 + |v(E_B)|^2 \right] |c_\sigma(E_B)|^2 e^{-2\text{Im}[q_{ez}(E_B)]z} \quad (\text{S23})$$

and

$$|\Psi_\sigma^h(z \geq 0)|^2 = \left[ |u(E_B)|^2 + |v(E_B)|^2 \right] |d_\sigma(E_B)|^2 e^{-2\text{Im}[q_{ez}(E_B)]z} \quad (\text{S24})$$

valid in the right superconductor, respectively.

As mentioned, for each solution  $\Psi$  with positive energy  $E_B$ , there is simultaneously also a second solution of the Bogoljubov–de Gennes equation with negative energy  $-E_B$ . The corresponding wave function  $\tilde{\Psi}$  can be obtained from Eqs. (S9) and (S10) by interchanging  $u$  to  $-v^*$  and  $v$  to  $u^*$ ; for the corresponding tilde probabilities,  $|\tilde{a}_\sigma|^2$ ,  $|\tilde{b}_\sigma|^2$ ,  $|\tilde{c}_\sigma|^2$ , and  $|\tilde{d}_\sigma|^2$ , one obtains

$$\begin{aligned} |\tilde{a}_\sigma|^2 &= |a_{-\sigma}|^2, & |\tilde{b}_\sigma|^2 &= |b_{-\sigma}|^2, \\ |\tilde{c}_\sigma|^2 &= |c_{-\sigma}|^2, & |\tilde{d}_\sigma|^2 &= |d_\sigma|^2. \end{aligned} \quad (\text{S25})$$

Thus, the negative energy eigenstates  $\tilde{\Psi}$  have not only opposite spin, but due to  $u \mapsto -v^*$  and  $v \mapsto u^*$  also the opposite relative sign between the electron and hole components when compared to the positive energy eigenstates  $\Psi$ .

## II. DERIVATION OF THE QUASIPARTICLE DENSITY OF STATES

To compute the quasiparticle (QP) density of states (DOS) in the system, we adapt McMillan's method [S2], which allows us to construct the spin-resolved retarded Green's function  $G_\sigma^R(z, z'; E)$  directly from the incoming and

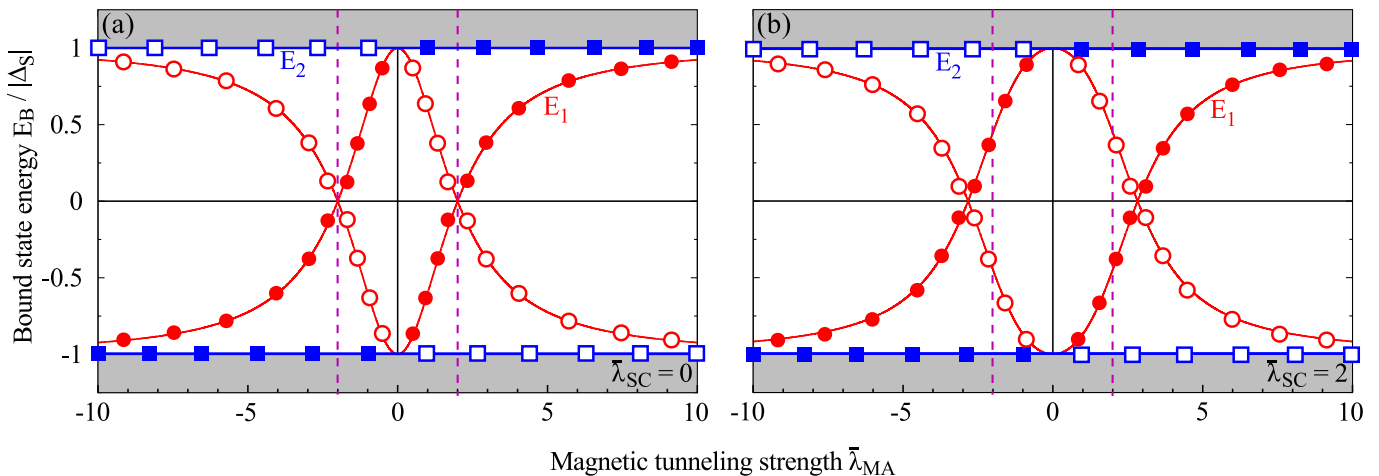


FIG. S3. Spin-resolved bound state energies  $E_1$  and  $E_2$  of the YSR (red) and the Andreev (blue) states as functions of the magnetic tunneling strength  $\bar{\lambda}_{\text{MA}}$  at zero phase difference. Values of the interfacial scalar tunneling are  $\bar{\lambda}_{\text{SC}} = 0$ , panel (a), and  $\bar{\lambda}_{\text{SC}} = 2$ , panel (b); Rashba SOC is absent. The dashed vertical lines signify the positions of zero-energy YSR-like states for the junction in panel (a). For additional scalar tunneling at the interface, panel (b), the zero-energy states shift to larger values of  $\bar{\lambda}_{\text{MA}}$ , in accordance with Eq. (5) in the manuscript. Filled (empty) boxes indicate spin up (down) Andreev states and filled (empty) circles spin up (down) YSR states, respectively.

scattered states. One can use Eqs. (S9)–(S10) and perform their analytical continuation to get the true incoming and outgoing (scattered) states. After some tedious calculations, we end up with

$$G_{\sigma}^{\text{R}}(z, z'; E) = -\frac{im}{\hbar^2 q_{\text{ez}} [|u|^2 - |v|^2]} \left\{ \left[ e^{iq_{\text{ez}}|z-z'|} + a_{\sigma} e^{-iq_{\text{ez}}(z+z')} \right] \begin{bmatrix} |u|^2 & uv^* \\ u^*v & |v|^2 \end{bmatrix} + b_{\sigma} e^{i(q_{\text{hz}}z - q_{\text{ez}}z')} \begin{bmatrix} u^*v & |v|^2 \\ |u|^2 & uv^* \end{bmatrix} \right\} \\ - \frac{im}{\hbar^2 q_{\text{hz}} [|u|^2 - |v|^2]} \left\{ \left[ e^{-iq_{\text{hz}}|z-z'|} + b'_{\sigma} e^{iq_{\text{hz}}(z+z')} \right] \begin{bmatrix} |v|^2 & u^*v \\ uv^* & |u|^2 \end{bmatrix} + a'_{\sigma} e^{i(q_{\text{hz}}z' - q_{\text{ez}}z)} \begin{bmatrix} uv^* & |u|^2 \\ |v|^2 & u^*v \end{bmatrix} \right\}, \quad (\text{S26})$$

where  $a_{\sigma}$  and  $b_{\sigma}$  are the previously introduced reflection coefficients for an incoming electron-like QP, and  $a'_{\sigma}$  as well as  $b'_{\sigma}$  their counterparts in case of an incident hole-like QP.

Finally, the QP DOS (at energies  $|E| \geq |\Delta_{\text{S}}|$ ) in the superconducting state is given by

$$\text{DOS}_{\text{S}}(E) = -\frac{1}{\pi} \text{Im} \{ \text{Tr} [G_{\sigma}^{\text{R}}(z, z; E)] \}. \quad (\text{S27})$$

This expression was evaluated in the manuscript close to the interface ( $z = 0$ ), where we also normalized the QP DOS to the related normal-state DOS,  $\text{DOS}_{\text{N}}(E)$ . The latter is obtained from the above expressions when setting  $u(E) = 1$  and  $v(E) = 0$ .

### III. BOUND STATE SPECTRUM ANALYSIS AND ZERO-ENERGY STATES

In this section, we shortly analyze how further parameter regimes—not studied in the manuscript—would affect the bound state energies. We again distinguish the two important limiting cases: the *Andreev* and the *Yu-Shiba-Rusinov* limit.

#### A. Andreev limit

In the absence of magnetic tunneling, the subgap bound states are solely formed by the conventional Andreev states, see Eq. (3) in the manuscript. Generally, the energies of those states can be tuned either by changing the strength of scalar tunneling  $\bar{\lambda}_{\text{SC}}$ —which effectively corresponds to changing the degree of interfacial transparency—or by altering the superconducting phase difference  $\phi_{\text{S}}$  by means of external magnetic fields. The Andreev-like subgap spectrum is shown in Fig. S2 as a function of  $\phi_{\text{S}}$  and for different strengths of  $\bar{\lambda}_{\text{SC}}$ ; since there is no magnetic tunneling and SOC

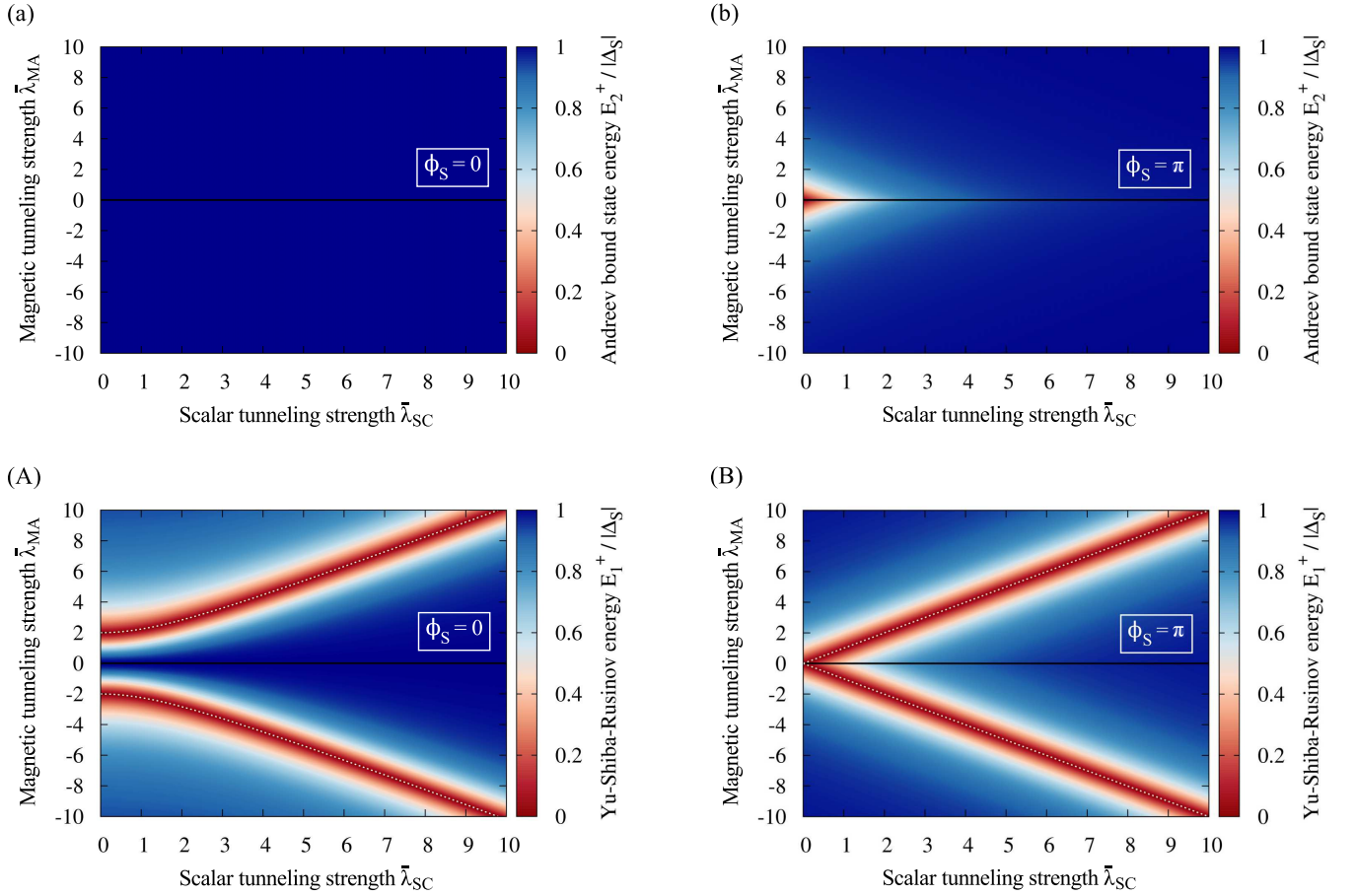


FIG. S4. (a) Bound state energies of the Andreev bound states as functions of  $\bar{\lambda}_{SC}$  and  $\bar{\lambda}_{MA}$  at fixed phase difference  $\phi_S = 0$ . The color code alters from dark-red (gap center) to dark-blue (gap edge) and we only show the positive bound state energies. (b) Same calculations for phase difference  $\phi_S = \pi$ . A clear formation of zero-energy Andreev-like states is visible for a small parameter region around the origin, referring to nearly perfectly transparent Josephson junctions. Panels (A) & (B) show similar calculations for the YSR-like states. Generally, the zero-energy YSR parameter space is much richer than the one for zero-energy Andreev-like states.

is not present, each Andreev state is doubly spin degenerate. For perfectly transparent junctions,  $\bar{\lambda}_{SC} = 0$ , Eq. (3) in the manuscript further simplifies to [S3, S4]

$$E_1^\pm = E_2^\pm = \pm |\Delta_S| \cos(\phi_S/2). \quad (\text{S28})$$

As a consequence, two Andreev branches cross at zero energy for all  $\phi_S = \pi \pmod{2\pi}$ . The formation of such zero-energy states attracted recently lots of attention, mainly in connection with the emergent Majorana modes [S5–S9]. However, the main experimental obstacle acting against these zero-energy Andreev modes is the required perfect junction transparency, which is still challenging to achieve in practice. Already for small, but finite  $\bar{\lambda}_{SC}$ , the zero-energy states disappear and the Andreev bound states shift towards energies close to the gap edges, approaching  $\pm|\Delta_S|$  in the limit of  $\bar{\lambda}_{SC} \rightarrow \infty$ . Nevertheless, the situation can become different for Josephson junctions on top of topological insulators. In such systems, Fu and Kane predicted [S10] an existence of topologically protected zero-energy Majorana states, which show robustness against disorder and also extraordinary transport properties like, for example, a  $4\pi$ -periodic Josephson current.

## B. Yu-Shiba-Rusinov limit

If there is no interfacial scalar tunneling and the S phase difference is tuned to zero, we effectively deal with a uniform bulk superconductor with an independent magnetic tunneling barrier in its center. In that case, we expect

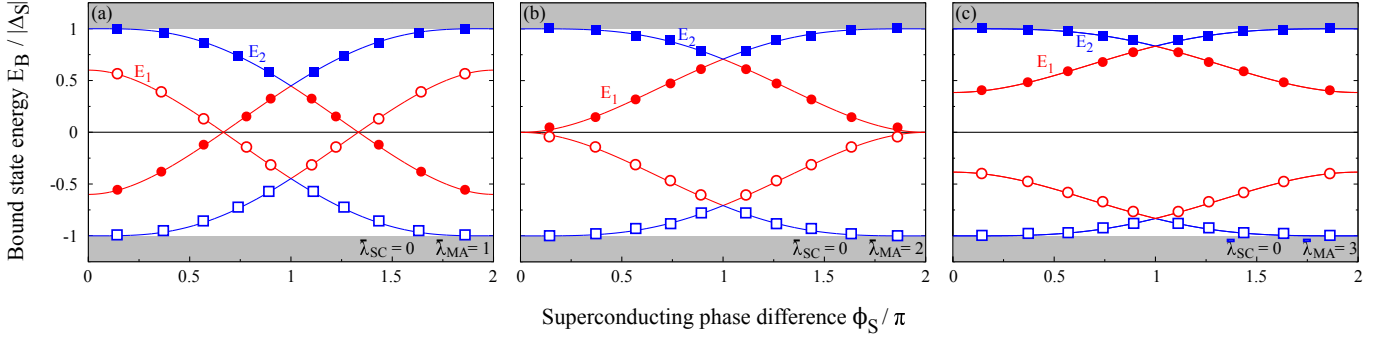


FIG. S5. Spin-resolved bound state energies  $E_1$  and  $E_2$  of the YSR (red) and the Andreev (blue) states as functions of  $\phi_S$  for scalar tunneling strength  $\bar{\lambda}_{SC} = 0$  and various magnetic tunnelings  $\bar{\lambda}_{MA}$  given in the plots; Rashba SOC is absent. Filled (empty) boxes indicate spin up (down) Andreev states and filled (empty) circles spin up (down) YSR states.

YSR bound states to form. Setting  $\bar{\lambda}_{SC}$  and  $\phi_S$  to zero, the bound state spectrum in Eq. (S8) reduces to the expression given in the manuscript,

$$E_1^\pm = \pm |\Delta_S| \frac{\bar{\lambda}_{MA}^2 - 4}{\bar{\lambda}_{MA}^2 + 4} \quad \text{and} \quad E_2^\pm = \pm |\Delta_S|. \quad (\text{S29})$$

Returning to dimensional  $\lambda_{MA}$  and identifying  $\rho(\mu) = 2m/(\pi\hbar^2 q_F)$  with the one-dimensional DOS per unit length at the Fermi level, one recovers in  $E_1^\pm$  exactly the bound state energies obtained by Yu, Shiba, and Rusinov; see Refs. [S11–S13]. Simultaneously, there is still the  $E_2^\pm$  branch, which is in this limit located at the gap edges, similarly as in the Andreev limit at  $\phi_S = 0$ . Because of that analogy, we introduced in the manuscript the convention to call the  $E_1^\pm$  branch of the subgap spectrum as the *YSR-like* and the  $E_2^\pm$  branch as the *Andreev-like* branch—even in the more general case when  $\bar{\lambda}_{SC}$  and  $\phi_S$  are nonzero.

The bound state spectrum corresponding to the YSR limit is displayed in Fig. S3(a). It shows the characteristic spin structure, whose qualitative discussion is provided in the manuscript; consult Fig. 3 there. The chosen strengths of  $\bar{\lambda}_{MA}$  vary from  $-10$  to  $10$  and cover both antiferromagnetic and ferromagnetic coupling scenarios. For  $\bar{\lambda}_{MA} = 0$ , we recover the (conventional) doubly spin-degenerate Andreev bound states located at the gap edges, while the energy branches start to split at finite  $\bar{\lambda}_{MA}$ . The YSR-like branches approach the center of the gap with increasing  $\bar{\lambda}_{MA}$  and cross zero energy at  $\bar{\lambda}_{MA}^{\text{crit.}} = 2$ , where the YSR eigenstates additionally ‘flip’ their spin. For stronger magnetic tunnelings, the YSR branches shift again towards the gap edges, resembling the situation in Fig. S2 for large  $\bar{\lambda}_{SC}$ . The Andreev branches are not affected in energy by a change of  $\bar{\lambda}_{MA}$  at zero phase difference; also their spin does not change with an increase of  $\bar{\lambda}_{MA}$  in sharp contrast to the YSR-like part of the spectrum.

### C. Interplay between Andreev and YSR-like states

After exploring the two limiting cases, we now concentrate on the combined situation. Motivated by Fig. S3(a), we again start with the case  $\phi_S = 0$ , i.e., an effective single bulk superconductor with scalar and magnetic tunneling in the center. In this case, Eq. (S8) reduces to

$$E_1^\pm = \pm |\Delta_S| \sqrt{\frac{(\bar{\lambda}_{SC}^2 - \bar{\lambda}_{MA}^2 + 4)^2}{(\bar{\lambda}_{SC}^2 - \bar{\lambda}_{MA}^2 + 4)^2 + 16\bar{\lambda}_{MA}^2}} \quad (\text{S30})$$

for the YSR-like branch and

$$E_2^\pm = \pm |\Delta_S| \quad (\text{S31})$$

for the Andreev branch. The calculated bound state spectrum in the case of generally nonzero  $\bar{\lambda}_{SC}$ ’s and  $\bar{\lambda}_{MA}$ ’s is displayed in Fig. S3(b) for  $\bar{\lambda}_{SC} = 2$ . Comparing Fig. S3(b) with the pure YSR limit in Fig. S3(a), we see that the additional presence of interfacial scalar tunneling does not qualitatively change the spectral characteristics and the

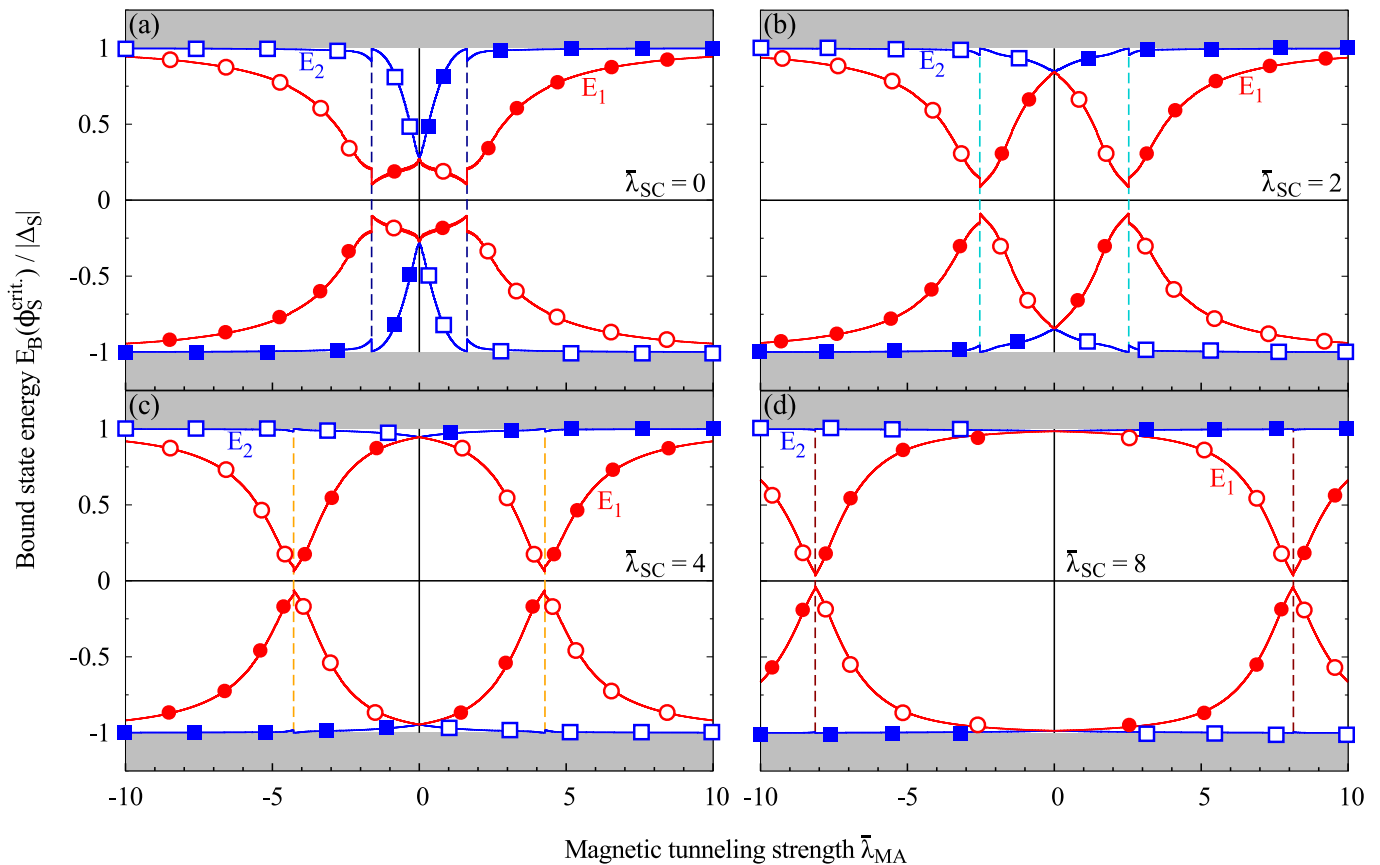


FIG. S6. Spin-resolved bound state energies  $E_1$  and  $E_2$  of the YSR (red) and the Andreev (blue) states as functions of the magnetic tunneling strength  $\bar{\lambda}_{MA}$  at the critical phase difference  $\phi_S^{\text{crit}}$ . Values of the interfacial scalar tunneling are (a)  $\bar{\lambda}_{SC} = 0$ , (b)  $\bar{\lambda}_{SC} = 2$ , (c)  $\bar{\lambda}_{SC} = 4$ , and (d)  $\bar{\lambda}_{SC} = 8$ ; Rashba SOC is absent. The dashed vertical lines emphasize the positions of magnetic tunneling induced transitions from 0 to  $\pi$  states. Filled (empty) boxes indicate spin up (down) Andreev states and filled (empty) circles spin up (down) YSR states.

spin structure of the underlying bound states. However, the presence of scalar tunneling naturally shifts the YSR-like branch more to the gap edges [S12] and, as another consequence, the points of zero-energy YSR crossings are shifted to larger  $\bar{\lambda}_{MA}$ 's—in the presented case to  $\bar{\lambda}_{MA}^{\text{crit}} = 2\sqrt{2}$  in accordance with Eq. (5) in the manuscript. In comparison with the Andreev limit, we see a general and experimentally positive trend: the presence of magnetic barriers gives rise to the formation of zero-energy YSR-like states, which are much more robust against “tunneling disorder” than their Andreev counterparts.

To illustrate the robustness of the zero-energy subgap states, Fig. S4 shows the spectrum for a wide range of tunneling parameters. To be specific, we show the positive Andreev and YSR-like bound state energies  $E_2^+$  and  $E_1^+$  as functions of  $\bar{\lambda}_{SC}$  and  $\bar{\lambda}_{MA}$  for  $\phi_S = 0$  and  $\phi_S = \pi$ , respectively. The corresponding negative counterparts of the spectrum (not shown) are simply  $E_1^- = -E_1^+$  and  $E_2^- = -E_2^+$ . As noticed in Sec. III A, the Andreev bound states are always located at the gap edges if there is no phase difference across the junction, independently of the actual strength of  $\bar{\lambda}_{SC}$ . The continuously dark-blue colored region in Fig. S4(a) shows the same behavior, now for any scalar and magnetic tunneling strength. If  $\phi_S$  gets tuned to  $\pi$ , see Fig. S4(b), and both scalar and magnetic perturbations are absent, we recover the mentioned zero-energy Andreev states (dark-red region), which are themselves extremely sensitive to weak perturbation in terms of finite  $\bar{\lambda}_{SC}$  or  $\bar{\lambda}_{MA}$ . The situation turns out to become more interesting for the YSR-like states, see Figs. S4(A) and (B). From Eq. (5) in the manuscript, we deduce that one can always find a  $\bar{\lambda}_{MA}$  for fixed values of scalar tunneling strength and S phase difference such that the YSR-like branches cross at the gap center, giving rise to zero-energy YSR states. The related parameter space for zero-energy YSR states is thus indeed much richer than for the conventional Andreev states as indicated by the dark-red regions in Figs. S4(A) and (B). For better visualization, the analytical condition for the formation of zero-energy YSR states, see Eq. (5) in the manuscript, is included as white dashed lines.

When discussing the phase dependence of the spectrum in the manuscript, we did not show the situation for

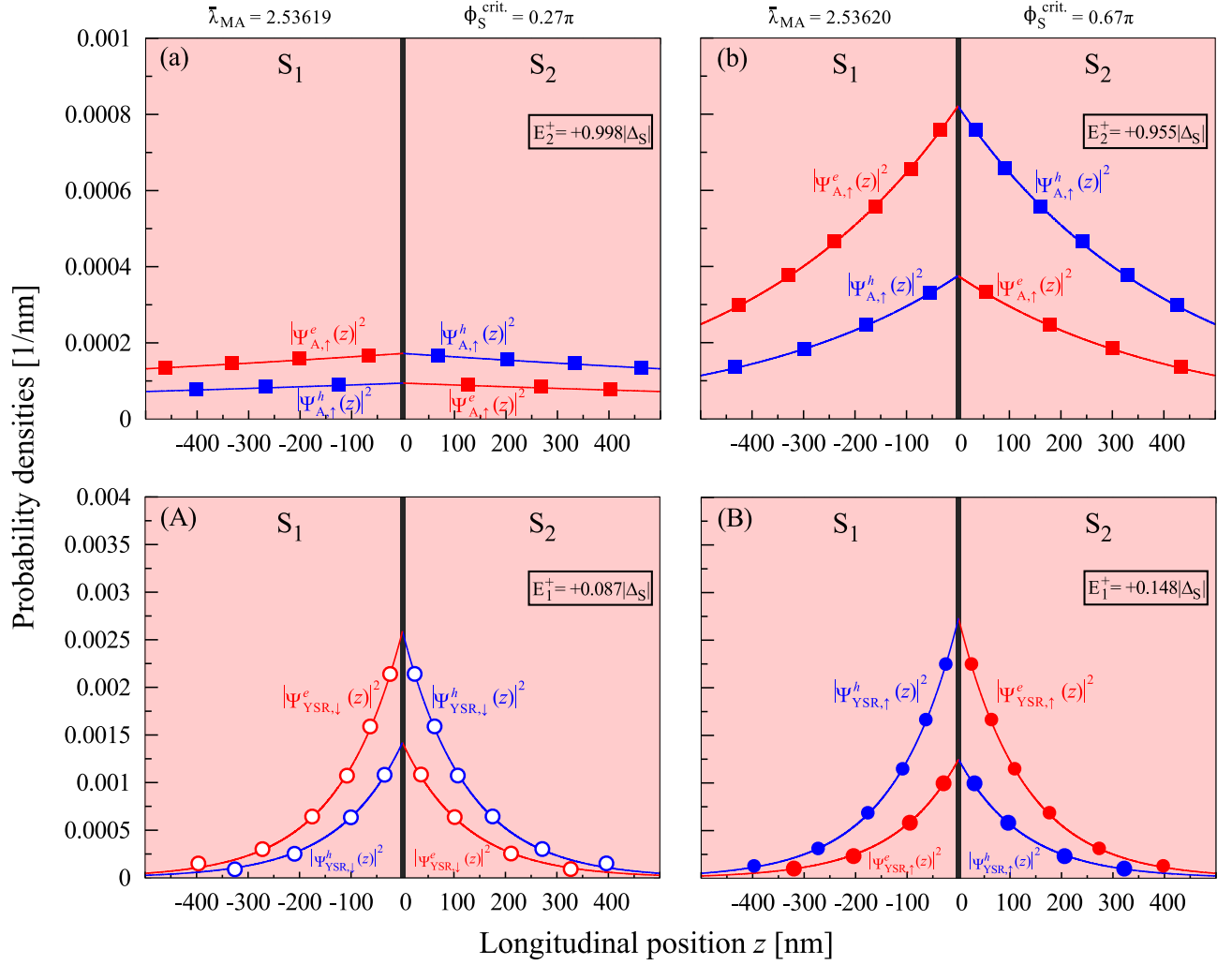


FIG. S7. Spatial profiles of spin-resolved and electron-hole separated probability densities for the Andreev (upper panel) and YSR (lower panel) bound states with positive energies. Scalar tunneling is fixed at  $\bar{\lambda}_{SC} = 2$  and the values of  $\bar{\lambda}_{MA}$  and  $\phi_S$  are tuned to points just before and after the  $0-\pi$  transition; Rashba SOC is not present. The figures at the left, panels (a) and (A), show the corresponding densities around the interface up to 500 nm for the  $0$  state, whereas the figures at the right, panels (b) and (B), show analogous data for the  $\pi$  state. The related junction parameters are listed at the upper margin; filled (empty) boxes indicate spin up (down) Andreev states and filled (empty) circles spin up (down) YSR states. Clear signatures for the  $0-\pi$  transition can be observed in the wave function behavior of the YSR-like states—the change of the spin ordering and the reversal of electron-hole content.

perfectly transparent junctions,  $\bar{\lambda}_{SC} = 0$ , as this is experimentally rather hard achievable. The related results are displayed in Fig. S5. Both the qualitative characteristics of the subgap states and their spin structure are the same as described in the manuscript. However, it is worth to mention that the Andreev and YSR-like states always cross at  $\phi_S = \pi$  as long as scalar tunneling is absent. The energies at which the two branches cross follow from the general spectrum, Eq. (S8), and are given by

$$E_{\text{cross}}^{\pm} = \pm |\Delta_S| \sqrt{\frac{\bar{\lambda}_{MA}^2}{\bar{\lambda}_{MA}^2 + 4}}. \quad (\text{S32})$$

#### IV. SPECTRUM AT THE CRITICAL PHASE DIFFERENCE

As briefly mentioned in the manuscript, it is more common from the experimental point of view to investigate the bound state spectrum by means of STM/STS spectroscopy not at zero superconducting phase difference, but instead

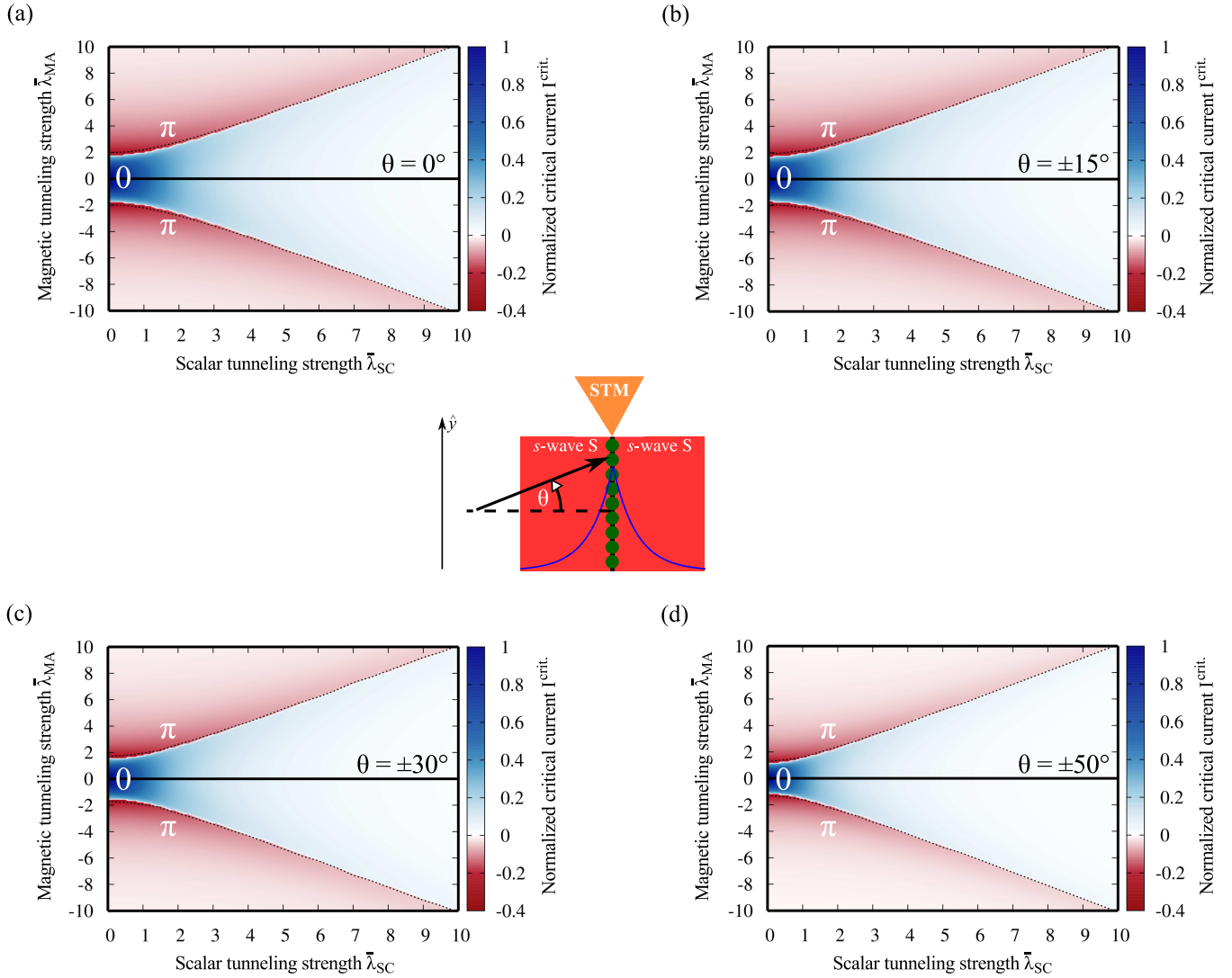


FIG. S8. Contour plot of the normalized critical current as a function of  $\bar{\lambda}_{\text{SC}}$  and  $\bar{\lambda}_{\text{MA}}$  in the absence of Rashba SOC at zero temperature. Blue and red regions represent 0 and  $\pi$  junction regimes. The transition lines separating the two phases are displayed by white borderlines; the parameters at which zero-energy YSR states emerge are shown by dashed lines. We consider effective 2D junctions in which the incident QPs enclose the angles (a)  $\theta = 0^\circ$ , (b)  $\theta = \pm 15^\circ$ , (c)  $\theta = \pm 30^\circ$ , and (d)  $\theta = \pm 50^\circ$  with the interface normal; for the definition of  $\theta$ , see the illustration in the center.

at the critical superconducting phase at which the maximal Josephson current flows through the system. Therefore, we present in Fig. S6 the energy level calculations as a function of the magnetic tunneling strength also for that particular scenario and for various scalar tunneling strengths. The qualitative features are the same as explained at zero phase difference. The ‘spin flips’ at the 0- $\pi$  transitions points (additionally emphasized by dashed lines) again fingerprint the quantum phase transition between the junctions’ 0 and  $\pi$  state.

## V. WAVE FUNCTION ANALYSIS

In the manuscript, we qualitatively explain the physical connection between the formation of zero-energy YSR-like states—indicating a quantum phase transition in the systems’ ground state—and the Josephson current reversing 0- $\pi$  transitions. Therefore, we analyzed the difference between electron-like and hole-like densities in the bound state wave functions, see Fig. 3 in the manuscript, and directly connected them to the Cooper pair transporting channels in the junction. For completeness, we here show the spatial profiles of the wave functions’ electron and hole components.

The procedure how to obtain  $|\Psi_{A,\sigma}^e(z)|^2$  and  $|\Psi_{\text{YSR},\sigma}^e(z)|^2$  for the Andreev and YSR-like states, respectively, is summarized in Sec. I. We checked various parameter regimes, observing the same qualitative features; therefore, we just present the results for one particular scalar tunneling strength, i.e., for  $\bar{\lambda}_{\text{SC}} = 2$ , see Fig. S7. The values of  $\bar{\lambda}_{\text{MA}}$  are chosen slightly below and above the  $0\text{-}\pi$  transition point, which for the regarded junction at zero temperature is numerically estimated to lie between 2.53619 and 2.53620. The Andreev states (upper panel) are spatially less localized than their YSR-like counterparts (lower panel) since their energies are typically closer to the gap edges ( $0 \lesssim E_1^+ < E_2^+ \lesssim |\Delta_S|$ ) and the plotted densities decay with the decay length  $\kappa = 1/\{2\text{Im}[q_{\text{ez}}(E_B)]\}$ , which increases with increasing energy. The second important observation is that the spatial electron-hole content of  $\Psi_{A,\sigma}(z)$  and  $\Psi_{\text{YSR},\sigma}(z)$  changes. While the electron-like character dominates at the left and the hole-like character at the right of the interface for both the Andreev and YSR-like states in the  $0$  state, the YSR states ‘flip’ their spin and—since the effective longitudinal momentum particles experience at the magnetic interface is spin-dependent through the  $\bar{\lambda}_{\text{MA}}$ -terms in our model Hamiltonian—also the electron-hole content of the states’ wave functions gets reversed in the  $\pi$  state; see calculations provided in Sec. I. This reversal leads to the reversal of the Josephson current flow as shown in Fig. 3 in the manuscript.

## VI. 2D AND 3D JUNCTIONS

In the manuscript, we focused for simplicity on quasi-1D junctions grown along the  $\hat{z}$  direction, what allowed us to find closed analytical formulas. Here, we emphasize that the discussed characteristics—the connection between zero-energy YSR states and  $0\text{-}\pi$  transitions—persist also in 2D or 3D junctions. Figure S8 shows the normalized critical current for a 2D junction with a nonzero incident transversal momentum along the  $\hat{y}$  direction. This transversal momentum is described by an angle  $\theta$ , which the incoming electron-like QP forms with the interface normal. We present numerical calculations for  $\theta = 0^\circ$ ,  $\theta = \pm 15^\circ$ ,  $\theta = \pm 30^\circ$ , and  $\theta = 50^\circ$ , respectively. With increasing  $\theta$ , the critical  $\bar{\lambda}_{\text{MA}}$  supporting zero-energy YSR states slightly decreases. This can be anticipated from the analytical formulas for the 1D case provided in the manuscript. The tunneling parameters there need to be replaced by effective ones,  $\bar{\lambda}_{\text{SC}} \mapsto \bar{\lambda}_{\text{SC}}/\sqrt{1 - \sin^2\theta}$  and  $\bar{\lambda}_{\text{MA}} \mapsto \bar{\lambda}_{\text{MA}}/\sqrt{1 - \sin^2\theta}$ , to treat 2D junctions (and analogously for 3D junctions). As mentioned, the coincidence between forming zero-energy YSR states and the  $0\text{-}\pi$  transitions remains clearly visible also for nonnormal incidence.

- 
- [S1] P. G. De Gennes, *Superconductivity of Metals and Alloys* (Addison Wesley, 1989).  
[S2] W. L. McMillan, Phys. Rev. **175**, 559 (1968).  
[S3] C. W. J. Beenakker, Phys. Rev. Lett. **67**, 3836 (1991).  
[S4] A. A. Golubov, M. Y. Kupriyanov, and E. Il’ichev, Rev. Mod. Phys. **76**, 411 (2004).  
[S5] Y. Oreg, G. Refael, and F. von Oppen, Phys. Rev. Lett. **105**, 177002 (2010).  
[S6] M. Duckheim and P. W. Brouwer, Phys. Rev. B **83**, 054513 (2011).  
[S7] V. Mourik, K. Zuo, S. M. Frolov, S. R. Plissard, E. P. A. M. Bakkers, and L. P. Kouwenhoven, Science **336**, 1003 (2012).  
[S8] L. P. Rokhinson, X. Liu, and J. K. Furdyna, Nature Phys. **8**, 795 (2012).  
[S9] S. Nadj-Perge, I. K. Drozdov, J. Li, H. Chen, S. Jeon, J. Seo, A. H. MacDonald, B. A. Bernevig, and A. Yazdani, Science **346**, 602 (2014).  
[S10] L. Fu and C. L. Kane, Phys. Rev. Lett. **100**, 096407 (2008).  
[S11] L. Yu, Acta Phys. Sin. **21**, 75 (1965).  
[S12] H. Shiba, Progr. Theoret. Phys. **40**, 435 (1968).  
[S13] A. I. Rusinov, ZhETF Pis. Red. **9**, 85 (1968).